



Self-consistent implementation of a zero-equation transport model into a predictive model for a Hall effect thruster

Thomas A. Marks*

University of Michigan, Ann Arbor, MI, 48109

Alejandro Lopez Ortega † and Ioannis G. Mikellides ‡

Jet Propulsion Laboratory, California Institute of Technology, Pasadena, CA 91109

Benjamin A. Jorns. §

University of Michigan, Ann Arbor, MI, 48109

The performance of an axisymmetric multi-fluid Hall thruster code that incorporates a self-consistent, data-driven closure model for the anomalous electron transport is investigated. Five different operating conditions of the H9 magnetically shielded Hall thruster are simulated with the Jet Propulsion Laboratory's Hall2De. In order to capture the inherent uncertainty associated with the closure model, O(100) simulations are run for each condition, each of using a coefficient set sampled randomly from a probability distribution. The results of these simulations provide probabilistic predictions of thruster performance quantities including thrust, and discharge current, as well as several component efficiencies and centerline plasma properties. The model is found to yield converged solutions at all conditions, with large 10 kHz-range oscillations and performance trends with voltage and flow rate similar to experiment. The model under-predicts the thrust by 15-25% and over-predicts the discharge current by 20% on average compared to experiments at the same discharge voltage and mass flow rate. This performance discrepancy is due to lower beam utilization, mass utilization, and divergence efficiency than experiment, resulting from high Hall parameters in the acceleration region, which lead to a protracted ion acceleration region. The physical processes underlying this result are discussed in the context of future data-driven modeling efforts.

Nomenclature

\hat{z}	= axial coordinate
\hat{r}	= radial coordinate
$\hat{\theta}$	= azimuthal coordinate
\mathbf{E}	= electric field vector
\mathbf{B}	= magnetic field vector
ϕ	= electrostatic potential
q_s	= charge of species s
m_s	= mass of species s
\dot{m}_s	= mass flow rate of species s
ω_{cs}	= cyclotron frequency of species s
T_s	= temperature of species s
n_s	= Number density of species s
P_s	= pressure of species s
\mathbf{u}_s	= velocity vector of species s
\mathbf{j}_s	= current density vector of species s
ν_{st}	= momentum-transfer collision frequency between species s and species t
ν_{AN}	= anomalous electron collision frequency

*PhD. Candidate, Department of Aerospace Engineering, Student Member AIAA

†Member of the Technical Staff, Electric Propulsion Group, 4800 Oak Grove Drive, Pasadena, CA, 91109, Mail Stop 125-109, Member AIAA

‡Member of the Technical Staff, Electric Propulsion Group, 4800 Oak Grove Drive, Pasadena, CA, 91109, Mail Stop 125-109, Fellow AIAA.

§Assistant Professor, Department of Aerospace Engineering, Associate Fellow AIAA

I. Introduction

HALL-effect thrusters are electric propulsion (EP) devices that feature moderate to high specific impulse and high thrust density compared to other conventional EP systems. This makes them attractive both as station-keeping thrusters for satellites as well as deep space thrusters for both robotic[1] and crewed[2, 3] missions. As the scope of missions employing Hall thrusters expands, the need for capable modeling and simulation (M&S) tools increases. This need is driven both by the desire to reduce qualification testing time for long-duration missions and to explore design space to develop thrusters with new levels of power and efficiency. One example of the utility of M&S tools is the recent development of magnetic shielding, the mechanism behind which was in part discovered using simulations[4, 5], and which has been responsible for a dramatic increase in Hall thruster lifetime[6].

Despite the utility of M&S tools, there remain unsolved problems in Hall thruster physics and operation which preclude the development of fully-predictive simulations. Most notably, in the crossed-field plasma in the thruster's annular channel, electrons diffuse across the confining magnetic field lines orders of magnitude more quickly than expected from classical theory[7]. This "anomalous" process has a profound influence on the structure of the Hall thruster plasma, governing key aspects of efficiency and acceleration. While many theories have been proposed for this effect, there is an emerging consensus that it is largely attributed to the presence of the growth of kinetically-driven micro-instabilities which produce an effective drag on the electrons[8]. The challenge from an M&S perspective is thus how to self-consistently model the effect of these modes in a thruster code.

With that said, while high-fidelity kinetic modeling is a valuable tool in directly capturing the physics of the processes driving the anomalous transport, the high computational expense makes them infeasible for practical engineering simulations of whole thrusters. We are therefore interested in fluid models of this transport. These offer a drastic reduction in computational cost, but their reduced fidelity means they will not be able to self-consistently capture the inherently kinetic nature of this anomalous transport. This motivates the need to develop approximate models of the anomalous transport which can be represented in a fluid framework.

Historically, the enhanced electron transport is represented in a fluid framework via the introduction of an effective transport coefficient—typically in the form of an anomalous electron mobility or anomalous electron collision frequency [7]. There is a long history of attempts to develop self-consistent models of the anomalous collision frequency, from Bohm diffusion[9], to algebraic (zero-equation) turbulence models[10–13], to more complex turbulence models consisting of a system of partial differential equations[14]. To date, however, none have proved predictive across multiple thrusters and operating conditions[15]. Practically, this has posed a major impediment for M&S of Hall thrusters. Without a validated model of the anomalous collision frequency, it is impossible to determine how a given thruster will perform from its geometry and operating conditions alone. The development of such models is thus of paramount importance to future Hall thruster M&S efforts.

In order to develop models which are applicable to a wide variety of thrusters and operating conditions, we have started exploring a data-driven approach to try to find an expression for the electron transport coefficients. In the first work in this vein, Jorns[15] used symbolic regression on a dataset of anomalous collision frequencies inferred from experimental measurements to propose algebraic closure models for this coefficient. In this work, the author was able to produce several models capable of predicting the anomalous collision frequency profile of a thruster not in the training data with greater accuracy than previously-proposed first principles models. However, the models were not self-consistently implemented into a Hall thruster simulation, so it was unclear whether these predictions would yield converged simulations with thruster performance and plasma properties similar to experiment.

To address this outstanding question, in a follow on work [16], we used an external loop to implement one of these models into Hall2De, a state of the art fluid Hall thruster code developed at the Jet Propulsion Laboratory[17]. We simulated the H9, a 9-kW class magnetically shielded thruster[18], and compared the model predictions to experimental results. We found that the integrated model resulted in a converged simulation with features qualitatively similar to experiment for a thruster not in the training dataset. We also obtained probabilistic predictions by drawing samples from an inferred distribution of model fit coefficients and running simulations at each coefficient set.

While this work was an initial proof of concept of the utility of a data driven model, it had a number of limitations. First, the collision frequency model was not directly implemented into the code, instead relying on an external loop to monitor the simulation and progressively modify the input parameters. As a result, we had to specify the anomalous collision frequency predicted by the data-driven model as a piecewise-linear function along the channel centerline, which was then projected along the magnetic field lines using Hall2De's standard approach[17]. While the off-centerline scaling may not significantly impact the simulation results[19], the external loop likely reduced the coupling between plasma and anomalous collision frequency models, which could have affected the solution. As a second limitation, we

only examined one operating condition, and the number of cases we ran to generate statistics for the predictions was sparse with only twenty points. Lastly, we did not consider the impact of the cathode anomalous collision frequency, which also may play an important role in governing the plasma dynamics in Hall thrusters[20, 21].

In light of the limited scope of the previous work, the need is apparent for a fully self-consistent implementation of the data-driven model into a Hall thruster simulation and for a more comprehensive evaluation of its predictive qualities. To this end, we expand the implementation of the data-driven closure model to be applied locally everywhere in the domain, making for a more self-consistent test. We also expand the dataset for comparison by simulating five operating conditions on the H9 magnetically-shielded Hall thruster for which we have experimental performance measurements. We improve the statistical estimates from our models as well by expanding the number of simulations to $O(100)$ per condition, each simulation using a coefficient set drawn from an inferred distribution. Lastly, we treat the scaling coefficient of the cathode anomalous collision frequency as uncertain, and sample from a distribution of this coefficient in concert with the other sampled model fit coefficients. This process yields probabilistic predictions of thrust, discharge current, anode efficiency, and centerline plasma properties at each condition, which are then compared to experiment.

This paper is organized in the following way. In Sec. II, we review the problem of electron transport in Hall thrusters and summarize previous attempts to model it in a fluid framework, including our own data-driven approach. In section III, we describe the model calibration procedure and review the capabilities and setup of our simulation. In section IV, we show probabilistic predictions for thrust, discharge current, specific impulse, and several efficiencies for the H9 at five operating conditions, and compare to experimental values. In section V, we discuss these results in the context of previous and future closure modelling attempts. Finally, in section VI, we summarize our findings.

II. The problem of anomalous electron transport in Hall thrusters

In this section, we discuss the nature of anomalous transport in the Hall thruster—both with respect to the channel and in the cathode near field. To this end, we first describe the geometry of the system and how transport is modeled in a fluid framework. We then outline closure models that have been proposed for both regions to date.

A. Cross-field transport in the channel

1. The closure problem

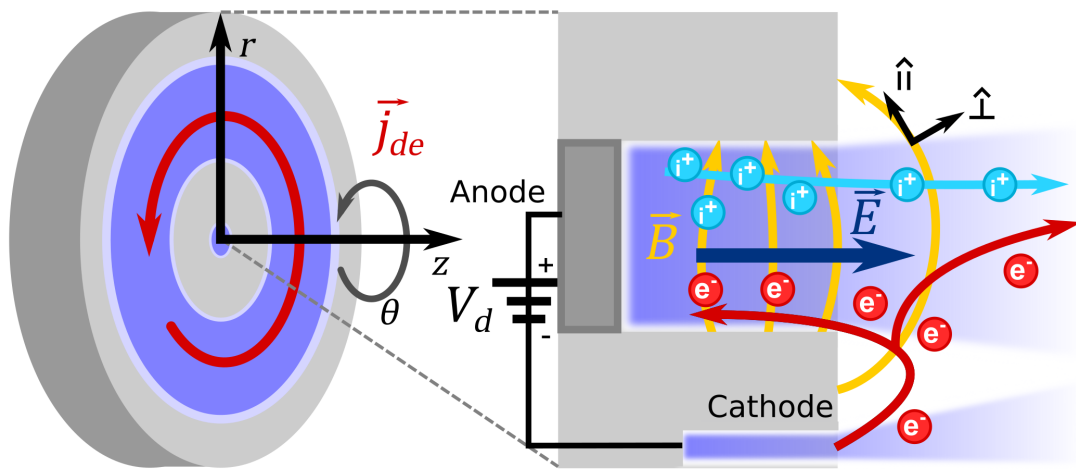


Fig. 1 Principle of operation of a Hall thruster illustrating relevant fields and drifts. \vec{E} is the electric field, \vec{B} is the magnetic field, \vec{j}_{de} is electron current, and V_a is the voltage applied to the anode. Ions (i^+) are in blue, while electrons (e^-) are in red. The field-perpendicular (\perp) and field-parallel (\parallel) coordinate vectors are indicated.

Figure 1 depicts the operation of a typical Hall thruster. Electrons streaming from a thermionic cathode toward the anode become trapped orbiting the radial magnetic field lines in the channel of the device, restricting their movement

toward the anode. The axial electric field created by the applied voltage orthogonal to the applied magnetic field induces a strong azimuthal *Hall current*. The high-speed electrons in this current impact and ionize neutral atoms injected into the channel. These ions follow the axial electric field, accelerating out of the device, while the plume is kept electrically neutral by the injection of additional electrons downstream from the cathode.

Although the electrons are highly-magnetized and in the ideal case confined to drifts strictly in the Hall direction, classical theory allows them to diffuse across the magnetic field lines via collisions with ions and neutrals. In a fluid formulation, this process is typically represented (neglecting electron inertia) with a generalized Ohm's law:

$$j_{e\perp} = \frac{e^2 n_e}{m_e \nu_e} \frac{1}{1 + \omega_{ce}^2 / \nu_e^2} \left(E_\perp + \frac{\nabla_\perp P_e}{en_e} \right) \quad (1)$$

In this equation, e is the fundamental charge, m_e is the electron mass; ω_{ce} is the electron cyclotron frequency (eB/m_e); ν_e is the classical electron collision momentum-transfer collision frequency, which is the sum of the electron-ion (ν_{ei}) and electron-neutral (ν_{en}) collision frequencies; n_e is the electron number density; E_\perp is the cross-field component of the electric field, and $\nabla_\perp P_e$ is the cross-field electron pressure gradient. We see that when $\omega_{ce}/\nu_e > 1$, increasing ν_e directly increases the cross-field electron current $j_{e\perp}$. The classical forms for the electron-ion and electron-neutral collision frequencies in this expression are known[22] and as such it is possible to calculate the classically expected cross-field electron transport in these devices. The problem of "anomalous" cross-field transport stems from the fact that experiments have shown that the cross-field electron transport is several orders of magnitude in excess of what classical collisions alone would predict[7]. It is standard practice in fluid-based models for Hall thrusters to try to approximate this enhanced transport by introducing an ad-hoc collision frequency e.g.

$$\nu_e \approx \nu_c + \nu_{AN}.$$

Here, $\nu_c = \nu_{ei} + \nu_{en}$ and represents the classical contributions to the total electron collision frequency, and ν_{AN} is the anomalous collision frequency coefficient. This coefficient can be changed and adjusted until simulation results for the electrons (and by extension other plasma properties) match experimental measurements. This is the current practice done in both hybrid particle-in-cell[23, 24] and fluid Hall thruster simulations[17, 19]. While this approach allows simulations to match experimental measurements with a high degree of accuracy[5, 25], it introduces a challenge for making predictions. Indeed, introducing this new parameter opens the plasma governing equations, leaving us with one more variable than we have equations for. Ideally, just as there are closed form solutions for classical collisions, we would want a similar one for the non-classical effects.

In this work, we are interested in zero-equation closure models for the anomalous collision frequency. A "closure model" is an expression or formula for an unknown quantity which makes the number of equations equal to the number of unknowns in a system, and which is in terms of quantities already being modelled by the existing governing equations. The simplest closure model would be one which assumes that the unknown quantity is constant, while more complex ones depend on the plasma properties. A "zero-equation" model is a model which takes the form of an explicit expression for a quantity of interest, in contrast to one-equation or two-equation models which require the solution of additional partial differential equations[14]. There is a long history of attempts to capture anomalous transport with a zero-equation closure derived from first principles, including models based on Bohm diffusion[9, 24], wall effects[7, 26, 27] and plasma turbulence[10–12]. However, none of these models has been fully-predictive or extensible between thrusters, so we turn to data-driven methods to discover new models of this phenomenon.

2. Adopted closure model

In a recent effort, Jorns[15] has proposed to apply data-driven methods to address the closure problem. Using a set of hand-tuned anomalous collision frequency profiles for a number of different thrusters as a dataset and employing symbolic regression, Jorns found at least three candidate models which performed better than previous first-principles closures. However, these closures featured numeric fit parameters which did not have clear physical meaning. Additionally, these models were inferred from steady-state one-dimensional thruster data, so it remained unclear how well these models would perform when integrated into a full time-resolved Hall thruster simulation. In this work, as in our last work[16] we focus on the simplest of the three candidate models, which we reproduce below:

$$\nu_{AN} = \omega_{ce} \left(c_0 + \frac{c_1 |\mathbf{u}_i|}{c_2 c_s + v_{de}} \right). \quad (2)$$

In this model, the anomalous collision frequency scales with the electron cyclotron frequency, the magnitude of the ion velocity $|\mathbf{u}_i|$, and inversely with the ion sound speed c_s and the electron $\mathbf{E} \times \mathbf{B}$ drift speed in the azimuthal direction v_{de} . This collision frequency is applied in the field-perpendicular direction in the bulk of the Hall thruster discharge. In the cathode plume (defined as the location radially inward of $r = 0.8r_{c,in}$, where $r_{c,in}$ is the radial location of the inner channel at the thruster exit plane), we apply a different model for anomalous collision frequency.

B. Electron transport in the cathode plume

1. The problem of closure

Figure 2a depicts a centrally-mounted hollow cathode with its associated magnetic field and field-aligned coordinate system. Electrons emitted from the cathode stream outward along the magnetic field lines until they eventually encounter the main Hall thruster ion beam. Some of these electrons remain with the beam to keep it electrically neutral as it leaves the device, while the remaining others then stream toward the anode across the field lines.

As with the thruster channel, experimental and computation evidence have shown that anomalous collisionality is present in the plumes of hollow cathodes like those used in Hall thrusters[28, 29]. Experiments have shown that there are two primary types of anomalous electron transport in the cathode plume[29]. The first is ion-acoustic in nature and acts primarily along the magnetic field lines. The other results from azimuthally-propagating anti-drift waves[30] and yields cross-field electron transport. In this work, we consider the effect of the parallel transport only. In thruster models, the effect of this anomalous collision frequency on the electron dynamics can be represented with a generalized Ohm's law. In this case, however, the transport is considered in the parallel direction to the applied field:

$$\frac{m_e \nu_e}{e^2 n_e} j_{e\parallel} = E_{\parallel} + \frac{\nabla_{\parallel} P_e}{en_e}. \quad (3)$$

In this equation, we see that the field-aligned potential and pressure gradients E_{\parallel} and $\nabla_{\parallel} P_e$ scale with the anomalous collision frequency for a fixed density n_e and parallel electron current $j_{e\parallel}$. We can see from this equation introducing an additional anomalous collision frequency in the cathode plume can lead to steeper gradients in both pressure and electric field. This is consistent with experimental measurements. Indeed, it has been shown that incorporating anomalous transport in the cathode plume can significantly increase the agreement between Hall thruster simulations and experiments[20]. As is the case with the Hall thruster channel dynamics, however, introducing this additional collision frequency again opens the governing fluid equations. We therefore need to select a closure model for the cathode anomalous collision frequency.

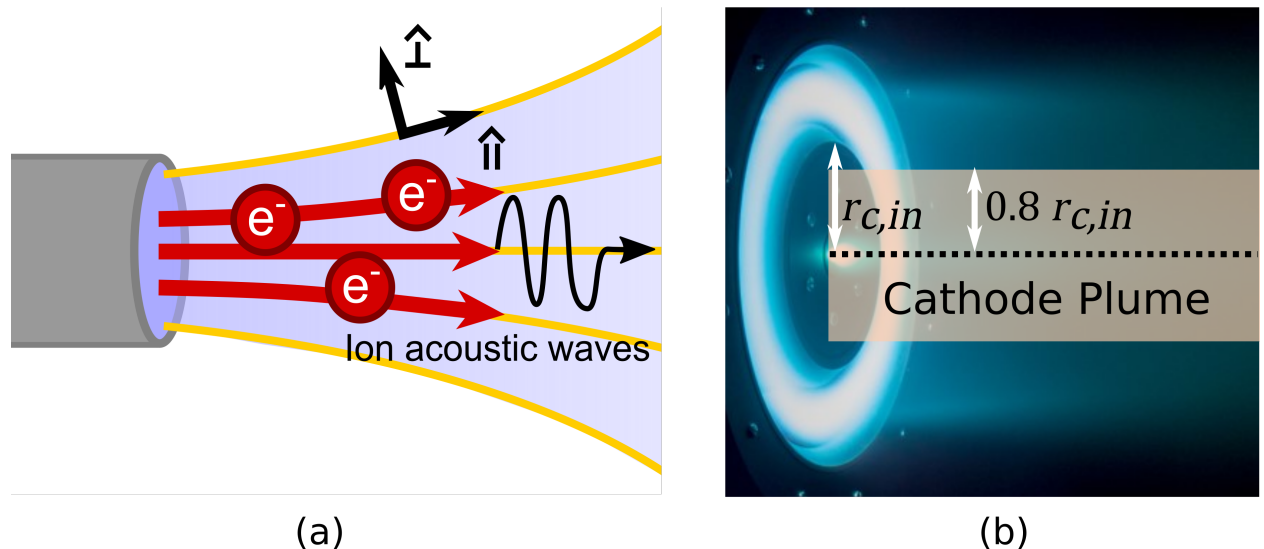


Fig. 2 (a) Magnetic field lines (yellow) and magnetically-aligned coordinate system of a centrally-mounted hollow cathode. Ion acoustic waves propagate primarily in the field-aligned direction. (b) The region of the plume in which the cathode anomalous collision frequency model is applied.

2. Adopted closure model

Following the work of Mikellides et al [28] and Jorns et al[29], we adopt a model for the transport based on the Sagdeev model[31]:

$$\nu_{AN, cathode} = \alpha M_e \omega_{pi} \frac{T_e}{T_i}. \quad (4)$$

Here, M_e is the electron Mach number, ω_{pi} is the ion plasma frequency, and α is a proportionality constant of order 0.01[32, 33]. In this model, the spectrum of the ion acoustic turbulence is saturated by nonlinear ion Landau damping. The wave grows linearly with the electron drift speed, leading to a dependence on the electron Mach number.

While it has been shown that this model may not be able to accurately capture oscillations in the cathode plume[21], it has been used with great success to improve the fit between experiment and simulation in hollow cathodes[28] and Hall thrusters[20]. In terms of actual implementation for this closure, unlike the case of the wave-driven effects in the Hall thruster channel, the IAT will not persist far downstream of the cathode. To represent this in practice, we therefore confine the region where this closure is adopted. This region is shown graphically in Fig. 2b. Outside this region, the anomalous cathode collision frequency is assumed to be negligible.

III. Methods

Now that the models for beam and cathode anomalous collision frequency have been established, we can describe our implementation of these models into a Hall thruster simulation. We first discuss how we determined the distribution of the model coefficients for both models. Next, we briefly describe the fluid code used in this work, the thruster we simulate, and the data to which we compare our results. Lastly, we describe the process by which we compute global performance metrics and efficiencies from the simulation output and tabulate simulation input parameters.

A. Model calibration

Both our data-driven model and the cathode anomalous collision frequency model have free parameters that must be calibrated against data. However, there is inherent uncertainty in the coefficients stemming primarily from uncertainty in the proposed model. We want to capture this rigorously and in turn be able to quantify how it impacts certainty in the integrated model predictions. To this end, we formulate our model calibration process as a Bayesian inference problem. In this approach, we represent the model coefficients, c_0, c_1 , etc. probabilistically, i.e. as distribution functions. The nature of these distribution functions can be inferred by comparing the model predictions to data. The algorithm for this is based Bayes' theorem (Eq. 5), where we obtain an expression for the probability P of that model parameters $\Theta = \{c_0, c_1, c_2\}$ being correct given our model f that we have observed the data d :

$$P(\Theta | d, f) = \frac{P(d | \Theta)P(\Theta | f)}{P(d)}. \quad (5)$$

Here $P(\Theta | d)$ is the *posterior probability*, or the probability of the model parameters being correct after seeing the data, given the model; $P(d | \Theta, f)$ is the *likelihood*, or the probability of seeing the data assuming the model parameters are correct, given the model; $P(\Theta)$ is the *prior probability*, or the probability of the model parameters being correct before seeing the data, and $P(d)$ is the *evidence*, or the probability of seeing the data.

1. Closure model for cross-field transport

In calibrating the our data-driven model, we take d to refer to the set of ten piecewise-linear calibrated anomalous collision frequency profiles from validated simulations described in Ref.[15]. This data spans three thrusters at multiple operating conditions, with powers ranging from 1 to 6 kW.

The prior probability, $P(\theta | f)$, encapsulates our knowledge of what the model coefficients should be prior to the inference procedure. In our previous effort [16], we took the priors to be uniform distributions on some interval. Here, we assume a more permissive Gaussian priors which allows the parameters to take any value. In the absence of more detailed information, we assume the prior probability of the coefficient set $\{c_0, c_1, c_2\}$ to be the product of three independent normal distributions centered on previous estimates of these coefficients. We use $c_0 = -0.0337$, $c_1 = 2.39$, $c_2 = 3.32$ as the mean of our prior distribution, as these were the coefficients initially described in Ref.[15]. We then have

$c_0 \sim \mathcal{N}(-0.0337, \sigma_{p0})$, $c_1 \sim \mathcal{N}(2.39, \sigma_{p1})$, and $c_2 \sim \mathcal{N}(3.32, \sigma_{p2})$. Here, σ_{pi} is the standard deviation of the prior distribution of parameter i . The overall prior probability density function for a model with N_p parameters with normal priors is given by

$$P(\theta) = \prod_{i=1}^{N_p} \frac{1}{\sigma_{pi}\sqrt{2\pi}} \exp\left[-\frac{1}{2} \left(\frac{\theta_i - \mu_{pi}}{\sigma_{pi}}\right)^2\right]. \quad (6)$$

The prior standard deviation of coefficient i , σ_{pi} , is a hyperparameter, an uncertain number which is not formally part of the parameter set being inferred. Tuning hyperparameters from data is a nuanced problem [34–36] and one outside of the scope of this work. Instead, we simply assume $\sigma_p = 3.0$ for all three parameters, which gives the prior distributions a similar variance to the previous work without explicitly constraining them to a fixed range of values.

As in our previous work, we assume that the likelihood, $P(d|\theta, f)$ is Gaussian in form. The full expression for our likelihood is:

$$P(d | \Theta, f) = \frac{1}{N} \sum_{i=1}^{10} \sum_{j=1}^N \frac{1}{\sigma\sqrt{2\pi}} \exp\left[-\frac{1}{2} \left(\frac{\log_{10} \nu_{AN}(T_i, z_j) - \log_{10} f(\Theta, T_i, z_j)}{\sigma(T_i, z_j)}\right)^2\right]. \quad (7)$$

For each of the training datasets $\{T_1, T_2, \dots, T_{10}\}$ we have N grid points $\{z_1, z_2, \dots, z_N\}$ at which various surrogate plasma data, including the calibrated anomalous collision frequency, are known, and at which our model f for the anomalous collision frequency can be evaluated. At each grid point, we assume the data is prediction plus some Gaussian noise. $\sigma(T, z)$ is the standard deviation of this noise at axial location z on the centerline of thruster T . We infer the base-ten logarithm of the anomalous collision frequency so that we do not bias our predictions toward regions where the anomalous collision frequency is high. This is important because the anomalous collision frequency is typically low in the ionization and acceleration regions, and the solution is very sensitive to the value of ν_{AN} in this region[19]. Taking the logarithm of the anomalous collision frequency in the likelihood evaluation means a factor of two difference when $\nu_{AN} \sim 10^6$ Hz is treated the same as when $\nu_{AN} \sim 10^9$ Hz, prioritizing a solution which matches the data well at all orders of magnitude.

We adopt a three-zone model for the noise. Mikellides and Lopez Ortega have shown that Hall2De is insensitive to changes of the anomalous collision frequency of up to two orders of magnitude when $z/L \lesssim 0.65$ and up to a factor of two in the plume [19] $z/L \gtrsim 1.5$, where L is the thruster channel length. The noise model we use in this work weights these regions accordingly:

$$\sigma(T_i, z_j) = \begin{cases} 3\sigma_N & z/L < 0.65 \\ \sigma_N & 0.65 \leq z/L \leq 1.5 \\ 2\sigma_N & z/L > 1.5 \end{cases} \quad (8)$$

Here, the “base noise” σ_N is another hyperparameter, which we set to 2. The evidence, $P(d)$ is typically difficult to evaluate. However, if data d is fixed with respect to the model f and parameters Θ , it acts solely as a normalizing constant on the posterior probability. The Markov chain Monte Carlo methods we employ in this work can sample from un-normalized posterior distributions, so evaluating the evidence is unnecessary.

Armed with these inputs, we now have a prescription for evaluating the probability distribution of coefficients. To visualize these distributions and to obtain sample coefficient sets with which we can run simulations, we employ the Delayed-Rejection Adaptive Metropolis algorithm[37] to sample randomly from the distribution. Figure 3 shows the resulting joint and marginalized probability distributions for the model coefficients from Eq. 2 after drawing one million samples. The three histograms on the diagonal of Fig. 3 are the marginal probability density functions of each of the parameters c_0 , c_1 , and c_2 . These represent the overall probability of seeing each of the three parameters without reference to the other two parameters. The three plots in the bottom left of Fig. 3 represent the joint distributions of the coefficients with respect to each other, and show how, if at all, the coefficients are correlated. We can see that the joint distribution of c_0 and c_1 appears roughly ellipsoid, with the long axis pointing down and to the right. This indicates that c_0 and c_1 are negatively correlated, which, with reference to Eq. 2, makes sense, as a smaller (more negative) value of c_0 would require a larger value of c_1 to give a similar result. The other parameters appear uncorrelated, as their joint distributions are roughly circular in shape.

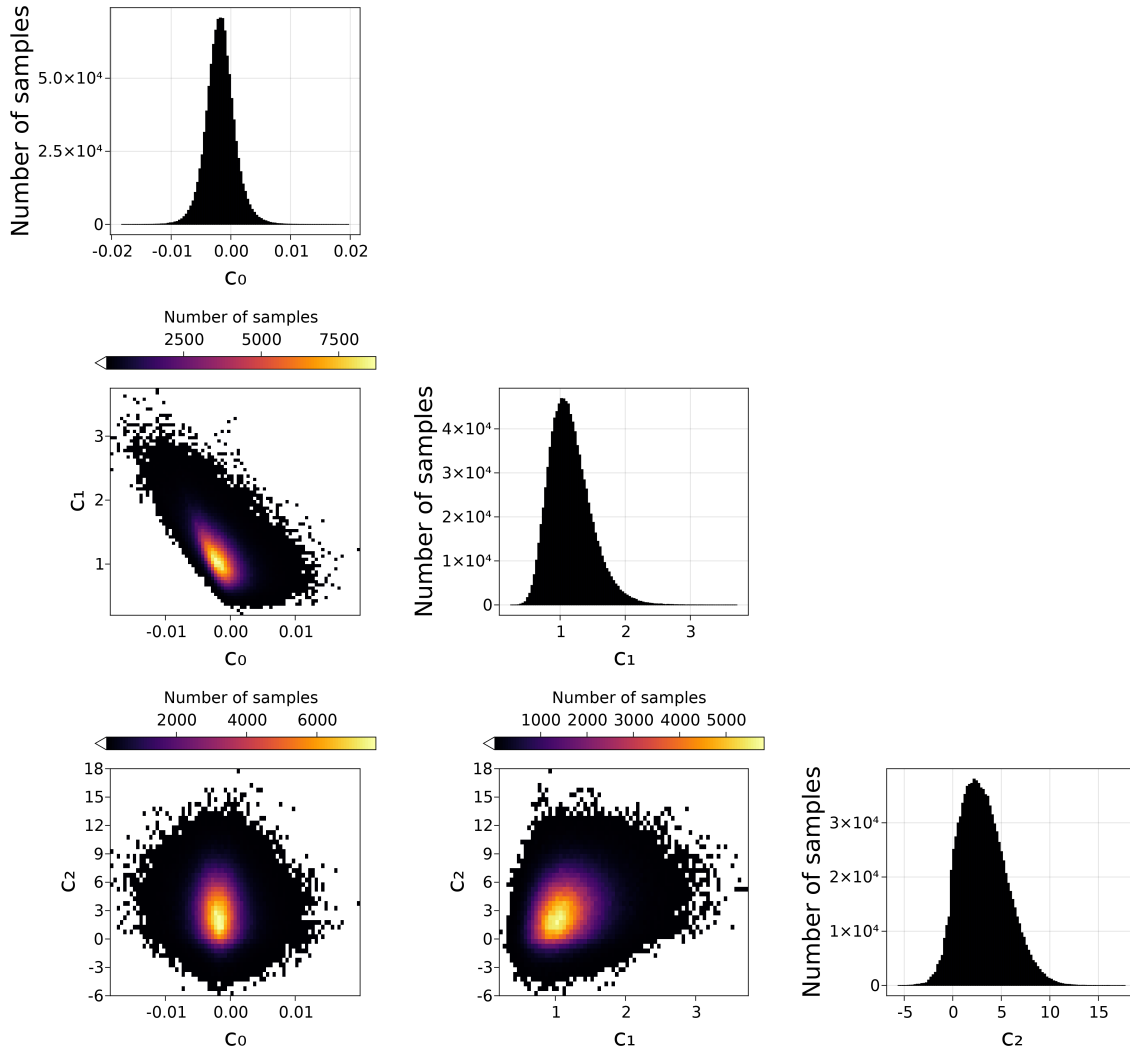


Fig. 3 MCMC posterior probability distribution function on the model coefficients. One million samples were drawn from the posterior. The acceptance percentage was 40%. Bright regions are regions of high probability (many accepted samples), while dark regions have low probability (few samples).

Using our probability distribution of fit coefficients, we can visualize how the variance in c_0 , c_1 , and c_2 affect the predictions of our model. To this end, we show in Fig. 4 the resulting predictions for the centerline anomalous collision frequency (along with 95% credible intervals) for two of the ten points in the training data. To generate these plots, we evaluate the model on the data at each sampled set of fit coefficients. At each grid point, we compute the median predicted value of ν_{AN} and a 95% high density credible interval (the smallest interval containing 95% of the predictions). We plot the median prediction of ν_{AN}/ω_{ce} in black and the credible interval in blue. The red dashed line represents the inferred anomalous collision frequency profile from the validated simulations that we were calibrating against.

The most probable coefficients according to our procedure are $\{c_0, c_1, c_2\} = \{-0.0015, 1.04, 2.16\}$, which differ somewhat from those obtained in Refs.[15, 16]. This can be attributed to the fact that our updated likelihood deemphasizes the downstream anomalous collision frequency in favor of a closer match in the acceleration region. This yields different fit coefficients. Fig. 4 depicts the worst fit among the ten produced, while Fig. 4 is among the better fits. We see that both fits agree well with the inferred anomalous collision frequency just downstream of the exit plane ($1 \leq z/L \leq 1.25$) while over-predicting the upstream collision frequency and under-predicting the downstream collision frequency. Referring to Fig. 3, we see that c_0 is typically very small, c_1 is close to unity, and c_2 is $O(5)$. Since the ion sound speed c_s is typically a few orders of magnitude smaller than the electron drift velocity v_{de} , we can simplify Eq 2

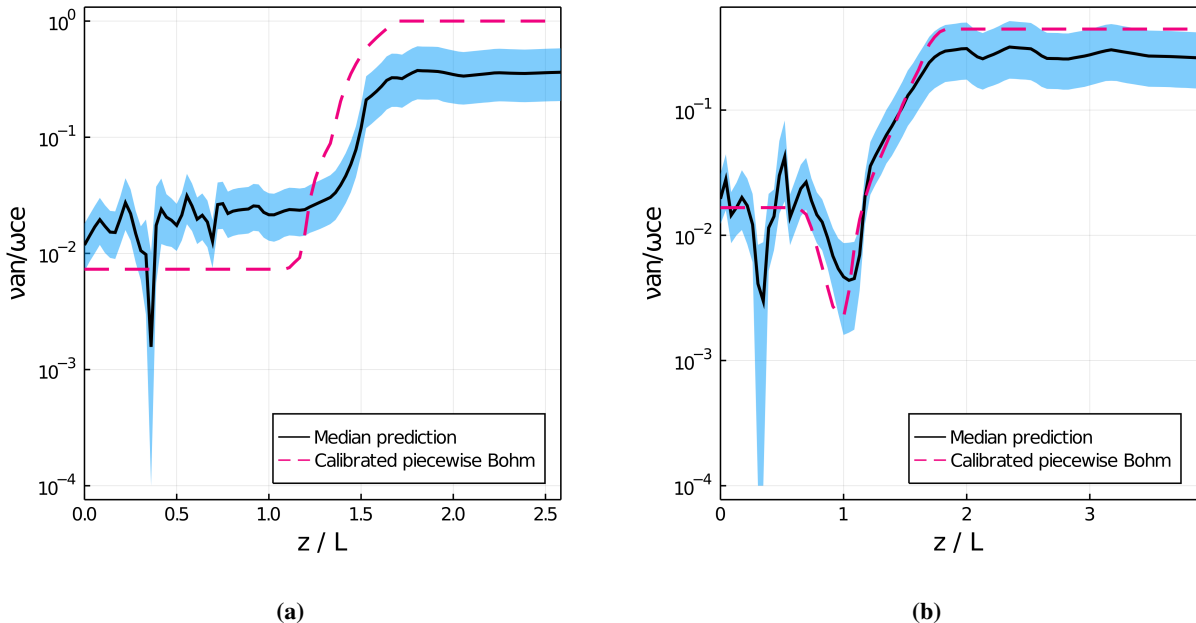


Fig. 4 Simulated centerline anomalous collision frequency profile as predicted by the data-driven model for thrusters 1 (a) and 5 (b) in the training data. The blue filled area represents 95% credible interval.

to show that our data-driven model scales with:

$$\frac{\nu_{AN}}{\omega_{ce}} \approx c_1 \frac{u_i}{v_{de}}.$$

This means that the goodness of fit is largely constrained by the ratio of the ion velocity to the electron drift velocity, and that the shape of the profile is insensitive to the coefficient choice. The coefficient with the largest impact, c_1 , only serves to scale the profile up or down. While we get a very good fit considering the simplicity of the model, the only coefficient with the ability to affect the shape of the curve, c_2 , has only a minor impact on the solution, so we fit some of the test data points (Fig. 4b) better than others (Fig. 4a).

2. Closure model for cathode plume

There is significantly less data available for calibrating the cathode anomalous collision frequency profile than for the beam collision frequency. The data we rely on for this work comes from Georgan and Jorns[21], who compared the predictions of several cathode anomalous collision frequency models to time-resolved measurements. They found a best fit coefficient of $\alpha = 0.003$ for the Sagdeev closure model which we employ in this work. (Eq. 4). In the absence of other data to compare against, we assume that $\log_{10}(\alpha)$ is normally distributed about $\log_{10}(0.003)$, with a standard deviation of a factor of three in either direction:

$$\log_{10}(\alpha) \sim \mathcal{N}(\log_{10}(0.003), \log_{10}(3)). \quad (9)$$

This distribution, while centered about the best fit point in Ref [21], encapsulates our uncertainty about α in two ways. First, other studies have found a value of $\alpha \sim 0.01$ gives good agreement between Hall thruster simulations and data [20] , and Eq. 9 gives significant probability weight in this region. Second, Georgan's data comes from the cathode employed in the H6 thruster[38], which is a slightly different cathode than the one used in the H9, the thruster we are simulating, so it is unreasonable to constrain our distribution of α too narrowly around his estimate.

B. Simulated thruster and operating conditions

All simulations in this work were performed using the geometry and magnetic field topology of the H9[18, 39], a magnetically-shielded Hall thruster developed in a partnership between the University of Michigan (UM), the NASA Jet

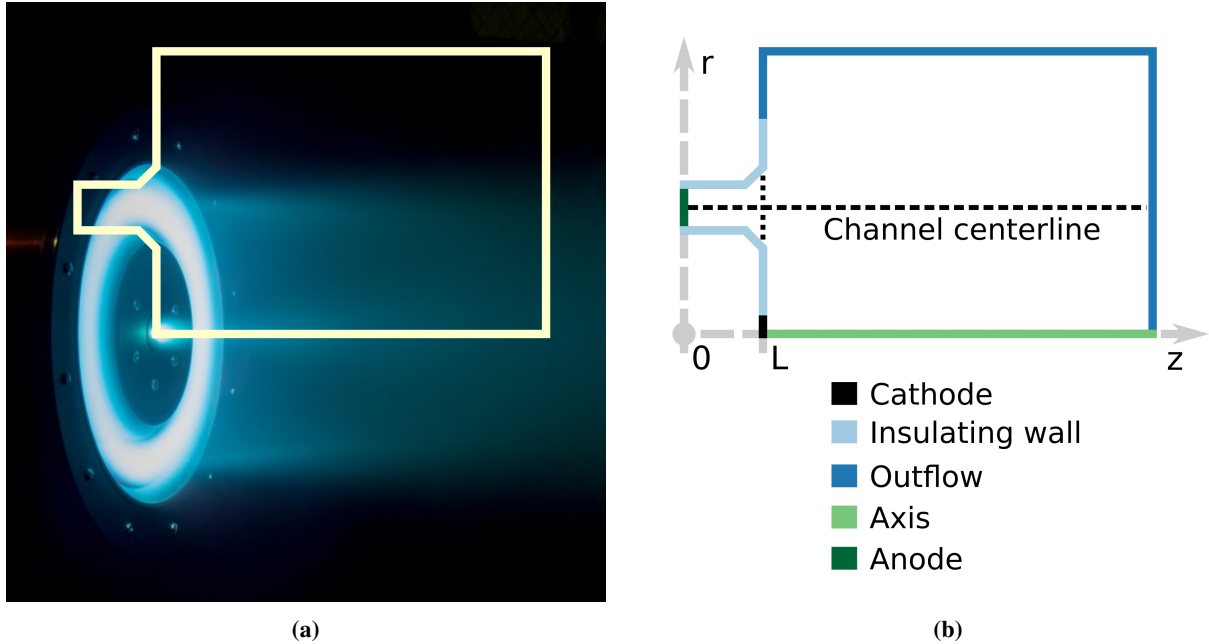


Fig. 5 a) H9 magnetically-shielded Hall thruster in operation with outline of computational domain and b) schematic of computational domain including all boundaries

Case	V_d (V)	I_d (A)	\dot{m}_a (mg/s)	T (mN)	P_b (Torr)	Simulations
1	300	15	14.8	292.9 ± 3.5	4.8×10^{-6}	100
2	300	20	18.5	377.6 ± 3.8	5.8×10^{-6}	98
3	400	15	15.4	350.8 ± 3.4	5.0×10^{-6}	99
4	500	15	16.1	405.1 ± 3.4	5.3×10^{-6}	97
5	600	15	15.4	447.2 ± 3.0	5.4×10^{-6}	100

Table 1 Experimental discharge voltage V_d , discharge current I_d , anode mass flow rate \dot{m}_a , measured thrust T , and measured background pressure P_b , and number of simulations for all test cases. Data from Ref. [40]

Propulsion Laboratory, and the Air Force Research Laboratory, and which was not present in the training dataset. A picture of the thruster with a depiction of the simulation domain, boundaries, and reference coordinate system is shown in Fig. 5. We examined five operating conditions, summarized in Tab. 1. Each case used xenon as the propellant. The performance data in this table was collected in 2021 at UM[40]. We compare our simulation results to both this data and laser-induced fluorescence measurements of the ion axial velocity in the acceleration region, collected at UM in 2018.

C. Description of Hall thruster model

Armed with our prescription for the data-driven model, distributions on its fit coefficients, and a thruster to simulate, we next turn to implementing our model self-consistently in a Hall thruster fluid model. To this end, following our previous work from Ref. [16], we used Hall2De, a two-dimensional axisymmetric fluid and particle-in-cell plasma code developed by the Jet Propulsion Laboratory. The details of its plasma model and solution procedure are described in detail elsewhere[17, 25]. In brief, Hall2De treats ions as unmagnetized and electrons as fully-magnetized and inertialess. Electrons are solved on a magnetic field-aligned mesh and ions can be solved either on the same mesh or on a separate Cartesian grid. We track three ion charge states (Xe^+ , Xe^{2+} , and Xe^{3+}) and two ion fluids (cathode ions and beam ions). The ions are assumed to be cold and their azimuthal motion is neglected. As the mean free path for neutral-neutral collisions is very long in Hall thrusters, they cannot be treated as fluid. Instead, they are treated using a line-of-sight viewfactor algorithm similar to those used in radiation transport computations[41].

Input	Value
Run time	6 ms
Time step	9 ns
Number of charge states	3
Number of ion fluids	2 (1 beam and 1 cathode)
Ion temperature	500° C
Cathode boundary electron temperature	5 eV
Cathode flow fraction	7%
Cathode ionization fraction	5%

Table 2 Simulation parameters

For the simulation boundary conditions, we assume that at insulating surfaces such as the channel walls and pole covers, as well as at the outflow boundaries, the net current and electric field are both set to zero. At conducting faces like the anode, a sheath forms and the electron current and potential are determined from the state of the plasma in the cell adjacent to the boundary edge. On the thruster centerline, all fluxes and gradients are set to zero to enforce axisymmetry. The electron temperature is set to 2.5 eV on the outflow faces, and its gradient is set to zero at all other faces, save for the cathode. The cathode boundary is a plasma source with user-provided mass flow rate, ionization fraction, and electron temperature. The cathode flow fraction is set to 7% to match experiment, but no data is available for the ionization fraction and electron temperature at the cathode keeper face. Parametric studies showed that the plasma solution was insensitive to these parameters, so we set them to 5% and 5 eV, respectively (see Appendix B).

We evaluate our data-driven model for the anomalous collision frequency on all field-perpendicular edges and in all cells. We specify the model coefficients in the simulation input file. For each operating condition, we sample 100 coefficient sets (c_0, c_1, c_2, α) from the data-driven coefficient distributions in Fig. 3 and the cathode anomalous collision frequency distribution Eq. 9. We set up a simulation input file for each of the coefficient sets, and then run a simulation using that input. Each simulation uses its case's pre-computed initial condition. These were generated by running cold starts at that case's flow rate and voltage for 0.5 ms of simulation time. The simulations are run in parallel on the Great Lakes supercomputer cluster at the University of Michigan. Each simulation uses 8 cores, and was run for 0.6 milliseconds of simulation time, at a timestep of 9 nanoseconds per iteration. Each batch of 100 parallel simulations took on average 15 hours to run. The simulation parameters discussed in this section are summarized in Tab. 2.

D. Computation of performance parameters

We briefly describe here how all performance metrics evaluated in the next section were computed from the simulation output. We compute the thrust, T , by integrating the ion axial momentum flux over the outflow boundaries:

$$T = \iint_{\text{outflow}} m_i n_i u_{iz} (\mathbf{u}_i \cdot \hat{\mathbf{n}}) dS. \quad (10)$$

Here, u_{iz} is the component of the ion velocity parallel to the \hat{z} axis, dS is the differential surface area, $\hat{\mathbf{n}}$ is the surface normal vector, and m_i is the ion mass. The discharge current I_d is found by integrating the sum of the ion and electron currents over the anode boundary:

$$I_d = \iint_{\text{anode}} (e n_i (\mathbf{u}_i \cdot \hat{\mathbf{n}}) - (\mathbf{j}_e \cdot \hat{\mathbf{n}})) dS. \quad (11)$$

With thrust and discharge current, we can compute the specific impulse I_{sp} and anode efficiency η_a :

$$I_{sp} = \frac{T}{g_0 \dot{m}_a} \quad (12)$$

$$\eta_a = \frac{T^2}{2 \dot{m}_a V_d I_d}. \quad (13)$$

Here, $g_0 = 9.81 \text{ m/s}^2$, \dot{m}_a is the mass flow rate through the anode, and V_d is the discharge voltage. These four parameters alone will give us a high-level overview of our thruster's performance, but in order to better characterize a thruster it is often useful to break the anode efficiency down into several components, following the model proposed by Hofer[42]:

$$\eta_a = \eta_m \eta_d \eta_b \eta_v \eta_q. \quad (14)$$

Here, η_m is the mass utilization efficiency, η_d is the divergence efficiency, η_b is the beam utilization efficiency, η_v is the voltage utilization efficiency, and η_q is the charge utilization efficiency. To compute these, we first need to compute the ion beam current, the axial component of the beam current, and the beam current fraction for each charge state. The beam current I_b and axial beam current I_{bz} are found by integrating the ion current density and axial ion current density, respectively, over the outflow boundaries:

$$I_b = \iint_{\text{outflow}} e n_i (\mathbf{u}_i \cdot \hat{n}) \, dS \quad (15)$$

$$I_{bz} = \iint_{\text{outflow}} e n_i u_{iz} (\hat{z} \cdot \hat{n}) \, dS \quad (16)$$

For a charge state j , the beam current fraction of that charge state Ω_j is found by integrating the beam current fraction of only that charge state:

$$\Omega_j = \frac{1}{I_b} \iint_{\text{outflow}} e n_{ij} (\mathbf{u}_{ij} \cdot \hat{n}). \quad (17)$$

In this expression, n_{ij} and \mathbf{u}_{ij} are the density and velocity of ions at charge state j . With these quantities in hand, we can compute our five efficiencies. We begin with the mass utilization, which is the ratio of the ion mass flow rate to the anode mass flow rate and measures how effectively the propellant is ionized:

$$\eta_m = \frac{\dot{m}_i}{\dot{m}_a} = \frac{m_i}{I_b} e \dot{m}_a. \quad (18)$$

The divergence efficiency measures how collimated the ion beam is and is given by the square of the ratio of the axial ion beam current to the total ion beam current:

$$\eta_d = \cos^2 \theta_d = \left(\frac{I_{bz}}{I_b} \right)^2. \quad (19)$$

The beam utilization efficiency represents what fraction of the discharge current is composed of ions, and is the ratio of the ion beam current to the discharge current:

$$\eta_b = \frac{I_b}{I_d}. \quad (20)$$

The voltage utilization efficiency represents how much of the discharge voltage is used to accelerate ions:

$$\eta_v = \frac{V_a}{V_d}. \quad (21)$$

Here, V_a is the effective “acceleration voltage” which is computed by averaging the ion kinetic energy over the outflow boundaries. Lastly, the charge utilization is a correction factor to account for multiply-charged ions:

$$\eta_q = \frac{\left(\sum_{j=1}^3 \Omega_j / \sqrt{Z_j} \right)^2}{\sum_{j=1}^3 \Omega_j / Z_j}. \quad (22)$$

Here, $Z_j = 1$ for singly-charged ions, 2, for doubly-charged ions, and 3 for triply-charged ions. Armed with these efficiencies, we are able to estimate the different contributions to Hall thruster performance and evaluate the impact of anomalous collision frequency models on the overall thruster performance.

IV. Results

In this section, we present the probabilistic predictions from our data-driven model of thruster performance, efficiency metrics and plasma parameters extracted from the thruster channel centerline. We begin by examining the distributions of thrust, specific impulse, discharge current, and anode efficiency at the 300 V and 15 A condition, then show how the median predictions of each of these metrics trend with voltage and flow rate. We then analyze several key efficiency metrics and the plasma properties along the thruster centerline to diagnose areas where the model may differ from experiment. Finally, we analyze the time-resolved behavior of our simulations.

A. Probability distributions for performance predictions at 400 V and 15 A

In Fig. 6, we present histograms of the predicted performance at the 400V and 15 A condition. The thrust is under-predicted, with a median thrust of 285 mN and a 95% credible interval of 210 - 310 mN, 19% lower than the experimental value of 350 mN (Tab. 1). The discharge current is over-predicted, with a median of 18 A (95% credible interval of 12 - 20 A) compared to the 15 A of the experiment. The low thrust leads to a low specific impulse, with a simulated median I_{sp} of 1900 s (95% credible interval 1500 - 2200 s) compared to 2350 s in the experiment. Finally, we find a median simulated anode efficiency of 39% (95% credible interval of 30-45%) compared to 65% in the experiment. The experimental thrust, efficiency, and specific impulse are not contained within the simulated credible intervals.

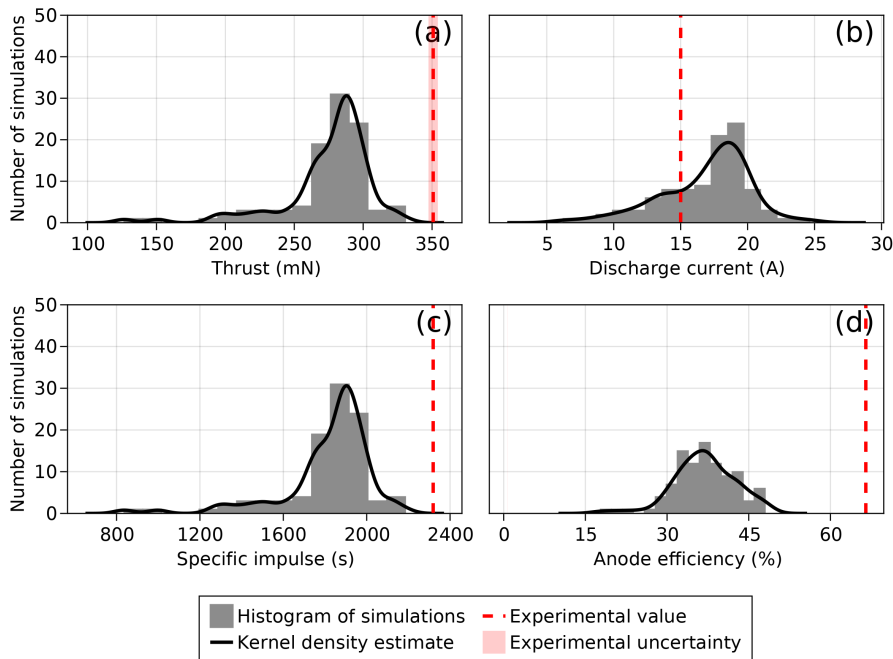


Fig. 6 Histograms of performance metrics at the 400 V and 15 A condition

B. Comparison of median performance metrics and experiment

To see how performance trends across voltages, we plot the median predictions and 95% credible intervals against the experimental data for all five conditions. Fig. 7. We see that, like the experiment, the thrust increases linearly with voltage and is underpredicted by 40-60 mN for all conditions except the 600 V and 15 A condition, where the thrust is underpredicted by 120 mN. For 300 V, 400V, and 500 V (at 15 A), the discharge current does not change significantly with voltage, which matches experiment, though the simulated discharge currents are 3 to 4 A higher than experiment. At 600 V and 15 A, the median discharge current drops to a value closer to experiment. Interestingly, at the 300 V and 20 A condition, the median simulated discharge current is predicted nearly exactly, though there is high uncertainty in this value. As I_{sp} scales linearly with thrust, we see the same trends as we see in the Fig. 7a, with a linear increase with voltage for all conditions except 600 V and 15 A. Finally, while the experimental the anode efficiency trends slightly upward at higher voltages, the median simulated anode efficiency trends slightly downward or remains flat.

In addition to accurately capturing the experiment trends with respect to voltage, our model also seems to predict the correct trends with increasing mass flow rate, though we only have two points to compare to (300 V and 15 A and 300 V and 20 A). The thrust increases with higher flow rate, though the increase in thrust in the simulation between 15 A and 20 A is only 40 mN, compared to a difference of nearly 100 mN in the experiment. As we would expect, the discharge current increases as well with increased flow rate, though again by a smaller magnitude than in the experiment (3 A in the simulation vs 5 A in the experiment for the same change in flow rate). The specific impulse and anode efficiency change little at higher flow rates in both simulation and experiment.

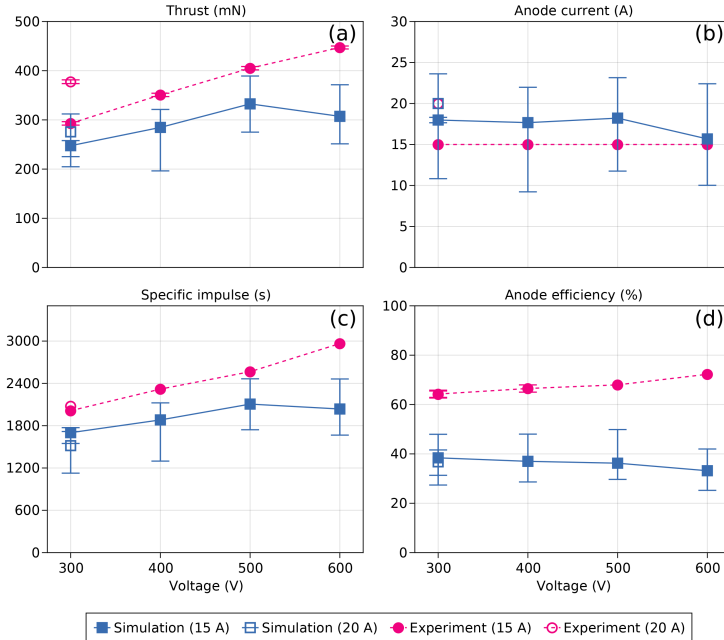


Fig. 7 Evolution of a) thrust, b) discharge current, c) specific impulse and d) anode efficiency with respect to discharge voltage for both simulation (blue) and experiment (magenta). The markers represent median predicted values and the uncertainty bars represent 95% credible intervals on the predictions.

With these figures in hand, we can summarize our data-driven model's predictive performance. We underpredict thrust by 40-75 mN at most conditions, overpredict the discharge current by 2-4 A, underpredict the specific impulse by 300-400s and underpredict the anode efficiency by less than a factor of two. However, with the exception of the 600 V and 15 A condition, we qualitatively reproduce experimental trends for thrust, specific impulse and discharge current with respect to both voltage and mass flow rate. We can now turn to analyzing what drives this lower performance.

C. Efficiency breakdown

To determine why the performance of the simulated thruster with our data-driven model is lower than experiment, we break down the thruster performance into component efficiencies, outlined in Sec. III.D. In Fig. 8, we show how our computed efficiencies compare to experimental values for the 400 V and 15 A. In this figure, we compute the anode efficiency from the thrust and discharge power, while the “probe” anode efficiency is the anode efficiency is the product of the other five efficiencies. We find that the charge and voltage utilization efficiencies are within uncertainty of experiment, while the mass utilization, beam utilization, and divergence efficiencies are significantly lower.

In Fig. 9 we present how these efficiencies change with voltages and flow rate. Note that we do not have experimental efficiency data for the 500 V and 600 V conditions. We see that that the median simulated mass utilization is flat with voltage, except for at the 600 V and 15 A condition, where it declines by 7% compared to the 500 V and 15 A condition. The beam utilization efficiency appears to trend up with voltage, though the 95% credible intervals do not significantly change, so it is statistically possible the beam utilization remains flat. The divergence efficiency is also uniformly lower than experiment, with only small variation at increasing voltage and flow rate. The charge and voltage efficiencies are very similar to experiment, with a median simulated charge efficiency 1-2% higher than experiment and a median

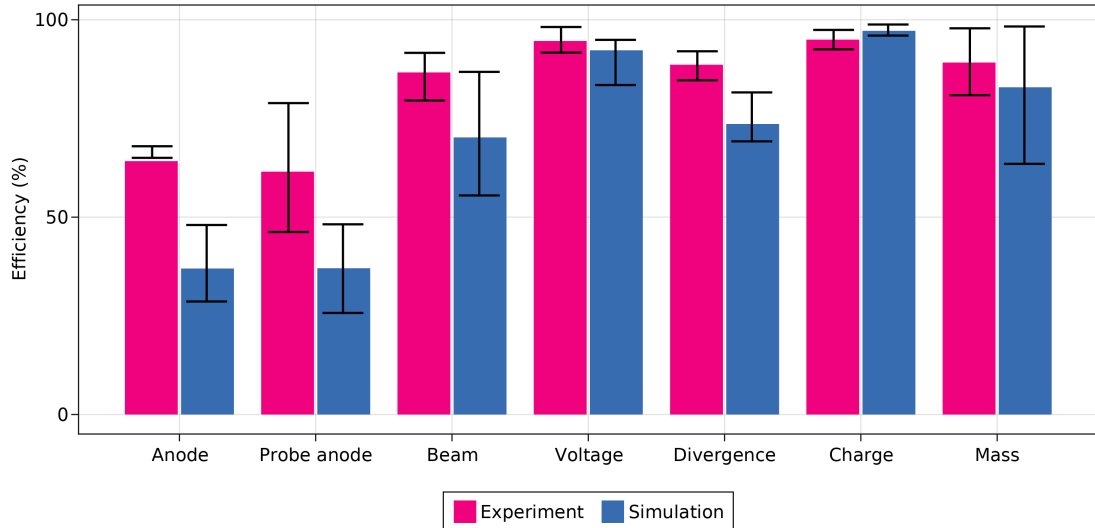


Fig. 8 Simulated (blue) and experimental (magenta) efficiencies at the 400 V and 15 A condition

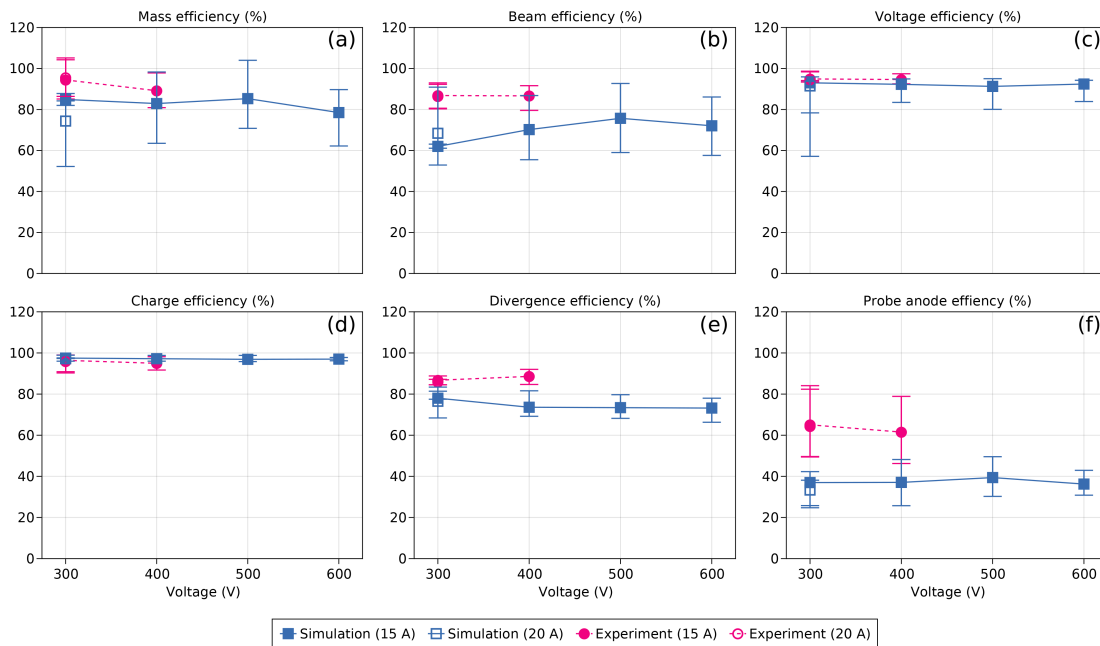


Fig. 9 Evolution as a function of discharge voltage of a) Probe anode efficiency, b) mass utilization efficiency, c) beam utilization efficiency, d) voltage utilization efficiency, e) charge utilization efficiency and f) divergence with respect to discharge voltage for both simulation (blue) and experiment (magenta). The markers represent median predicted values, and the uncertainty bars represent 95% credible intervals on the predictions.

simulated voltage efficiency 1-3% lower. The probe anode efficiency is consistent with the anode efficiency determined from the thrust and discharge power, indicating that our efficiency model captures all of the relevant factors affecting the thruster performance. The variance at 300 V and 15 A is significantly lower than at the other conditions.

In summary, the data-driven model predicts similar charge and voltage utilization efficiencies to experiment, but significantly reduced divergence, beam utilization, and mass utilization efficiencies. To understand why these efficiencies are low, we now turn to analyzing the centerline plasma properties.

D. Centerline plasma properties

In Fig. 10 we present simulated centerline profiles of the axial ion velocity, electric potential, normalized anomalous collision frequency, and electron temperature for the 400 V and 15 A condition. Compared to the laser-induced fluorescence measurements of ion velocity in Fig. 10a, we find that the simulated ion velocity profile is significantly more shallow than the experiment, with an ion acceleration region two thruster-lengths long. This is four times the length of the experimental region. Consistent with this more protracted acceleration, the potential profile in Fig. 10b is also shallow. The anomalous collision frequency profile (Fig. 10c) looks qualitatively similar to those in Fig. 4a and Fig. 4b, but axially-stretched and shifted downstream, with the inflection point occurring at 3 thruster-lengths downstream of the exit plane. Near the exit plane, at $z/L = 1$, the anomalous collision frequency is between 1/30 and 1 times the cyclotron frequency. This is unusual, as the anomalous collision frequency is typically $O(0.01)$ [19], a factor of two or three lower than the lowest value predicted by our model. Lastly, we see that the electron temperature curve is very wide, nearly three thruster-lengths in extent. It reaches a median peak of 45 eV at an axial location of $z/L = 2$, with a variance of nearly 75% in both directions.

While the variance in the anomalous collision frequency is approximately uniform throughout the domain, the variance in predictions at the 400 V and 15 A condition for ion velocity, plasma potential, and electron temperature reach their maximum in the acceleration region, and decline deeper into the plume. This holds true across all other conditions (seen in Appendix A), except for 300 V 15 A, where the variance in the acceleration region is much lower than the other conditions, but the variance in the far plume is much larger, with a ~ 150 V variance in the predicted potential drop.

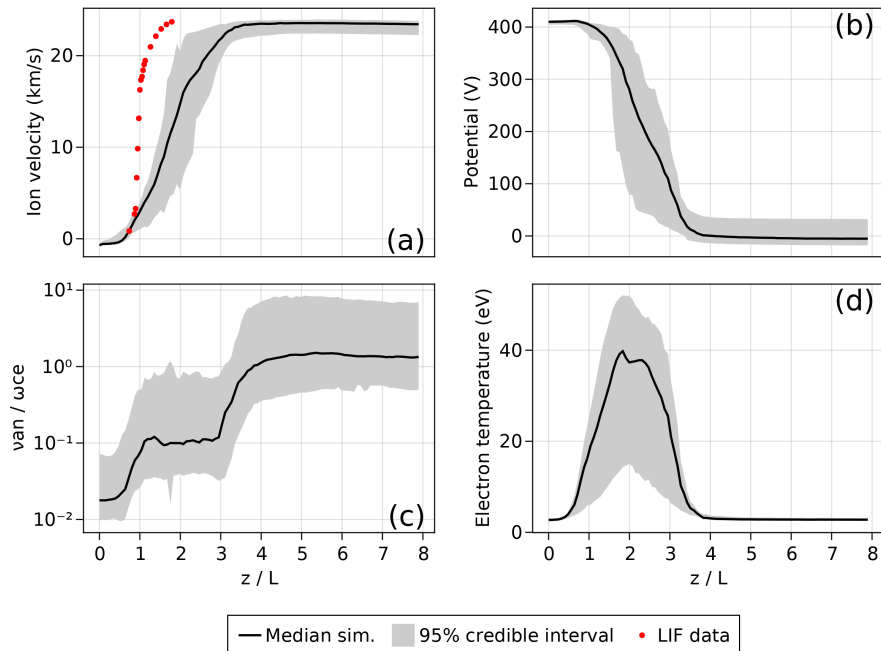


Fig. 10 Simulated centerline profiles of a) ion velocity, b) potential, c) normalized anomalous collision frequency and d) electron temperature at the 400V and 15 A condition. Ion axial velocity data obtained via laser-induced fluorescence is depicted as a dashed red line in (a)

E. Time-resolved analysis

Lastly, we examine the time-resolved behavior of our simulations and compare to experiment. Our last work found $O(10)$ kHz oscillations in the thrust and discharge current and axial displacement of the acceleration region in time with these oscillations, both of which are consistent with the well-known Hall thruster breathing mode[43]. We find a similar result in this study. In Fig. 11, we compare median and 95% credible intervals of the discharge current power spectra from our simulations to experiment, finding a 10 kHz-range oscillation in each case and qualitatively similar shapes. At 300 V and 15 A, we find a primary peak at 10 kHz, compared to 13 kHz in the experiment, with

a secondary higher-frequency oscillation at 35 kHz, compared to 47 kHz in the experiment. This may indicate a harmonic of the breathing mode[44] or some kind of ion transit time instability[7]. At 400 V and 15 A, the peaks are less well-defined in both simulation and experiment, with a simulated peak at a median value of 8 kHz compared to an experimental peak of 12 kHz. The other peaks are less well-defined in the experiment, while the simulation has a small secondary peak at 38 kHz. Finally, at 500 V and 15 A, we have median simulated peaks at 7 and 40 kHz compared to experimental peaks at 13, 64, 126, and 190 kHz. The latter two peaks are harmonics of the first peak and may be related to azimuthally-propagating cathode waves[30], which cannot be captured in an axisymmetric fluid code. Fig. 12b summarizes the trends in the simulated low-frequency oscillations. We see that the low frequency peak is uniformly about 5 kHz below the experimental peak, and that the 95% credible intervals in peak location allow for a shift of up to 5 kHz in either direction of the median. Fig. 12a shows that the median peak to peak amplitude of the simulated oscillations is a factor of two to three higher than the experiment, with 95% credible intervals containing oscillations of over 100 V for the two higher-voltage conditions.

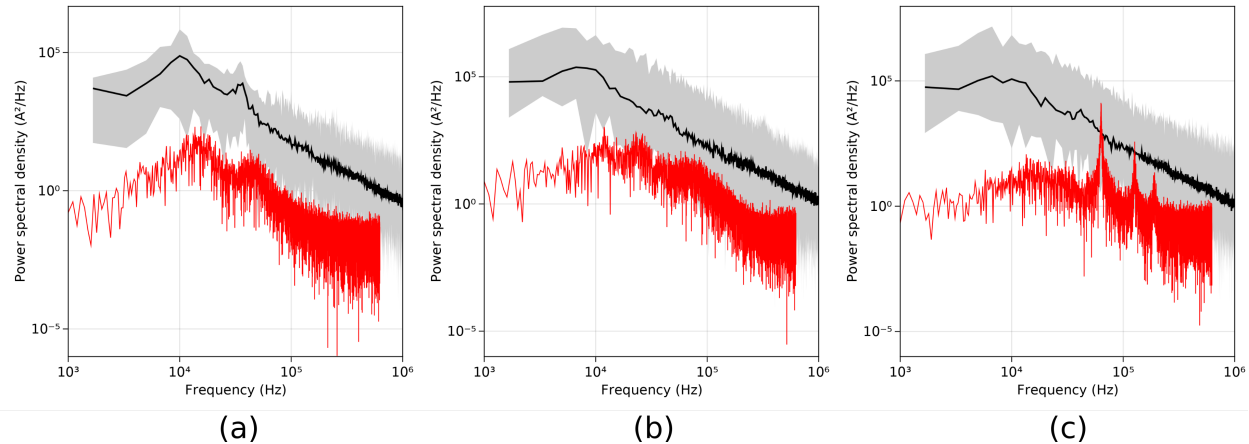


Fig. 11 Spectral densities of discharge current oscillations for the simulations (black) compared to experiment (red) at (a) 300 V and 15 A, (b) 400 V and 15 A, and (c) 500 V and 15 A. The grey filled area represents a 95% credible interval

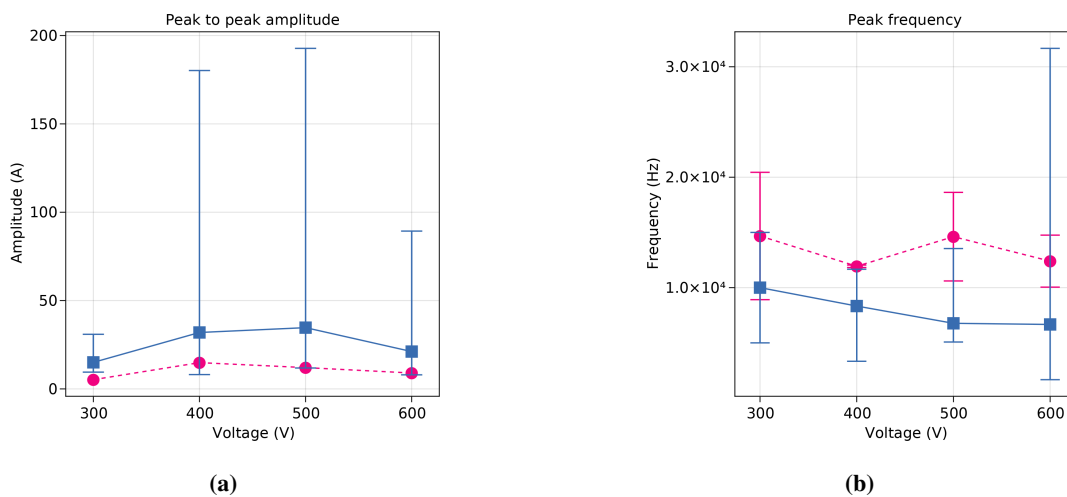


Fig. 12 Comparison of (a) peak to peak amplitudes (median and 95% credible interval) and (b) peak frequencies (less than 50 kHz) between simulation (blue solid line) and experiment (magenta dashed line)

The relatively wide variance in magnitude of the power spectra and peak to peak amplitude at each frequency compared to the median (around two orders of magnitude in some places) indicates that there are sets of coefficients

sampled for the data-driven models that may yield disparate oscillatory behavior. To illustrate this, we show in Fig. 13 representative time-resolved discharge current traces from three simulations at 400 V and 15 A to experiment. We see that the oscillation characteristics vary significantly with changes in the model coefficients. In Fig. 13a, the simulation qualitatively matches the experiment, albeit shifted upward. In Fig. 13b, the discharge current oscillations are large and coherent, with almost no high frequency content. Finally, in Fig. 13c the simulation is more quiescent, settling to a nearly constant discharge current after an initial oscillation. These variations in oscillatory state in part explain the wide variance in the power spectra shown in Fig. 11 and Fig. 12a. With that said, we note these significant variations in oscillation characteristics are not present in the 300 V and 15 A condition. This may in part explain why the variance in the model predictions of performance and acceleration region plasma properties is much lower at that condition (see Appendix A).

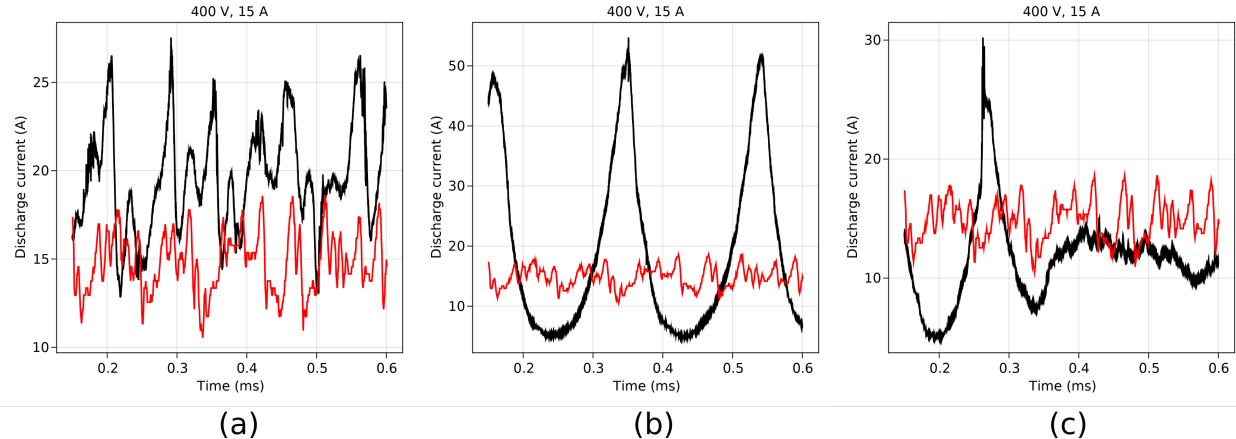


Fig. 13 Comparison of simulated (red) and experimental (black) discharge current oscillations for three simulations at 400 V and 15 A (a) ($c_0 = -0.00092, c_1 = 1.17, c_2 = 1.73, \alpha = 0.0044$), (b) ($c_0 = 0.0065, c_1 = 1.04, c_3 = 10.26, \alpha = 0.0031$), (c) ($c_0 = -0.0052, c_1 = 1.49, c_2 = 3.71, \alpha = 0.0032$)

V. Discussion

We now turn to discussing the results of our simulations and provide possible explanations for the discrepancies between our work and experiment. We then assess the impact of the cathode anomalous collision frequency on the variance in our results and finally assess the limitations and implications of our approach.

A. Physical explanation for low performance predictions from model

From the efficiency results in Sec. IV.C, it is clear that an increased plume divergence, low mass utilization efficiency, and decreased beam utilization efficiency are the main causes of the reduced total efficiency predicted by the model. We examine in this section the potential underlying causes for these discrepancies.

We first address the beam utilization efficiency. Starting with the steady-state electron fluid momentum equation and neglecting inertia, we arrive at a generalized Ohm's law, which describes how the electron current depends on the magnetic field strength, electric field, electron pressure gradient, and electron collision frequency:

$$(\nu_e + \nu_{AN}) \frac{m_e}{q_e} \mathbf{j}_e = q_e n_e \mathbf{E} + \nabla P_e - \mathbf{j}_e \times \mathbf{B} \quad (23)$$

Decomposing this into the field-parallel (\parallel), field-perpendicular (\perp) and azimuthal (θ) directions, we arrive at an expression for the electron current across the magnetic field (Eq. 25),

$$j_{e\parallel} = \frac{\Omega_e}{|B|} (q_e n_e E_{\parallel} + \nabla_{\parallel} P_e) \quad (24)$$

$$j_{e\perp} = \frac{1}{|B|} (q_e n_e E_{\perp} + \nabla_{\perp} P_e) \left(\frac{\Omega_e}{1 + \Omega_e^2} \right) \quad (25)$$

Here, we have introduced the Hall parameter Ω_e , which is equal to the ratio of the electron cyclotron frequency ω_{ce} to the total electron collision frequency $\nu_c + \nu_{AN}$. We can see that as the Hall parameter decreases toward 1 (as anomalous collision frequency increases), the cross-field electron current density grows substantially. Figure 10c shows that our model predicts that the Hall parameter should be between 1 and 30 near the exit plane (assuming $\nu_{AN} \approx \nu_c + \nu_{AN}$) in contrast to typical values of around 100[19]. This corresponds to a large increase in cross-field electron current in the acceleration region, which would increase the discharge current relative to the amount of plasma in the device. The beam utilization efficiency is the ratio of the ion beam current to the discharge current, so the increased discharge current at all of the 15 A conditions except 600 V that we observe in Fig. 7b would reduce the beam utilization efficiency. At the 600 V condition, the median discharge current is the same as experiment, but the thrust is lower than at the 500 V and 15 A condition, indicating that the ion beam current is likely low, which would also decrease beam utilization.

The low predicted Hall parameter in the channel and near the exit plane also has an impact on the ion beam divergence. We see in Fig. 10a and b that the ion potential gradient and thus electric field and ion acceleration profile are relaxed compared to both the data and the calibrated simulation. For a fixed electron current density and magnetic field strength, we can rearrange Eq. 25 to show that the electric field strength needed to get that amount of current across the field lines scales linearly with the Hall parameter for Hall parameters greater than 1 (Eq. 26), all else held equal:

$$(q_e n_e E_{\perp} + \nabla_{\perp} P_e) = j_{e\perp} |B| \frac{(1 + \Omega_e^2)}{\Omega_e}. \quad (26)$$

This equation shows that a low Hall parameter like we observe in our simulation will generally yield low electric fields, which would explain our results. To illustrate this, Fig. 14 compares a condition with a high peak electric field to one with a low peak electric field. The only difference between these simulations is the magnitude of the anomalous collision frequency near the exit plane. We see that a shallow potential gradient leads to a high beam divergence. Relating this back to our results, it is apparent that an anomalous collision frequency profile like the one predicted by our model produces shallow potential gradients, gradual ion acceleration, and low divergence efficiency.

Lastly, we address the low mass utilization efficiency. As can be seen in Fig. 10d, the median peak electron temperature predicted by our model this work at the 400 V and 15 A condition is 30 (95% credible interval 15-45) eV, compared to 50-60 eV in validated Hall2De simulations. These low electron temperatures likely result from a reduction in Ohmic heating as the small simulated Hall parameter leads to reduced cross-field impedance. This naturally leads to lower ionization rates and to lower mass utilization.

With a lower divergence efficiency and lower mass utilization efficiency, the reason for the low thrust compared to experiment becomes readily apparent. The amount of plasma being produced is lower overall, and the plasma that is produced is less axially-focused. This reduced mass utilization contributes to the low beam utilization efficiencies, as in addition to the discharge current being higher than experiment, the ion beam current is lower. The reduced mass utilization efficiency at 600 V and 15 A (Fig. 9a) is puzzling, given that the median electron temperature continues to climb from the 500 V 15 A condition. The reduction in plasma density that a lower mass utilization efficiency would imply is corroborated by the reduction in discharge current observed at this condition (Fig. 7b). This anomaly helps explain why the thrust is lower at that condition than would be expected by extrapolating the trend from lower voltages, and why the beam utilization efficiency is the same as the other conditions despite the discharge current being lower.

B. Effect of the cathode anomalous collision frequency on model predictions

One other factor that may impact the quality of our model predictions in the cathode model. This is an important consideration as well given that the uncertainty associated with this collision frequency model was not addressed in our previous work [16]. To quantify the effect of the variance in the cathode anomalous collision frequency on the variance in our model predictions, we perform a parametric study of thruster performance (discharge current and thrust) as a function of the cathode anomalous collision frequency scaling coefficient α at the 300 V 15 A condition. All other

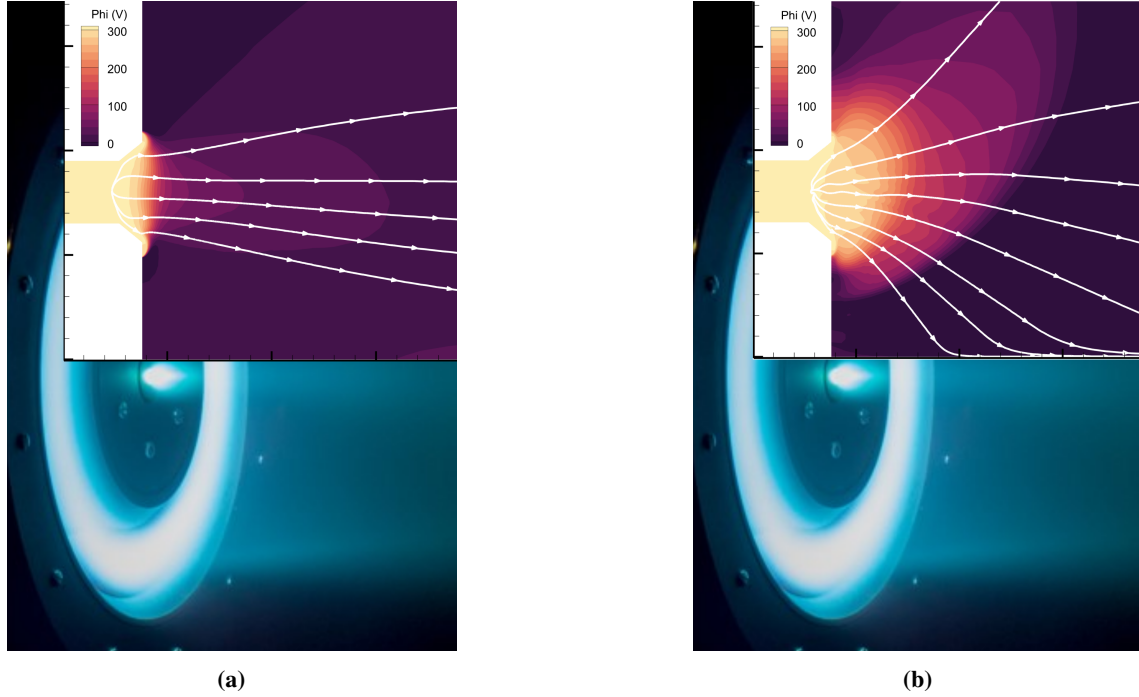


Fig. 14 Comparison of electrostatic potential (Φ) and ion streamlines (white lines) for two thruster simulations with (a) a steep potential gradient and narrow acceleration region (similar to experiment), and (b) a shallow potential gradient and wide acceleration region (typical of the model predictions in this work)

parameters were held constant. In Fig. 15 we show the results of this study and overlay the probability distribution for α used in this work. We find that the solution is insensitive to the cathode anomalous collision frequency over most of the distribution, with thrust and discharge current changing less than 10% within one standard deviation of the mean. Significant performance differences only begin to occur for $\alpha > 0.01$, a region encompassing only the upper 15% of the probability mass of our distribution, i.e. a one that is infrequently sampled. Thus, we can conclude the bulk of the variance in our predictions likely results from the variance in the ion beam anomalous collision frequency model and not in the cathode model.

C. Comparison to previous modeling efforts with data-driven closure

In a previous study, we performed a proof-of-concept assessment of the ability to integrate a data-driven model into Hall2De. This previous work had a number of limitations, however, including the fact that we only implemented the data-driven model only along the centerline of the thruster; we only simulated one condition (300 V and 15 A); and we only produced twenty samples from the posterior distribution. This work expands upon Ref. [16] in a number of significant ways. Most importantly, we implemented the anomalous collision frequency model directly into the Hall thruster simulation, which much more tightly couples the model to the plasma than the external loop approach previously adopted. We also drew five times more samples from the posterior distribution than in that work, giving us a much robust estimation of the distribution of our performance predictions.

As in the previous work, we find thrusts significantly below experimental values, although we find discharge currents 5-10 A higher than in the previous work. This yields an overall better match with the experimental discharge current, but results in a lower predicted anode efficiency. Other differences in this work include the axial profile of the various plasma parameters. Most notably, while Ref.[16] also showed a protracted acceleration region (an acceleration region about one thruster length in extent compared to one about half as long in experiment), the acceleration region length found in this work is two times larger. There are a few possible reasons to explain these differences in results. First, it is possible that some of the differences seen are due to radial effects on the structure of the acceleration region. In Hall2De, the anomalous collision frequency at a point off of the thruster centerline is found by following the magnetic field line passing through that point back to the centerline and scaling the centerline value of the anomalous collision frequency by

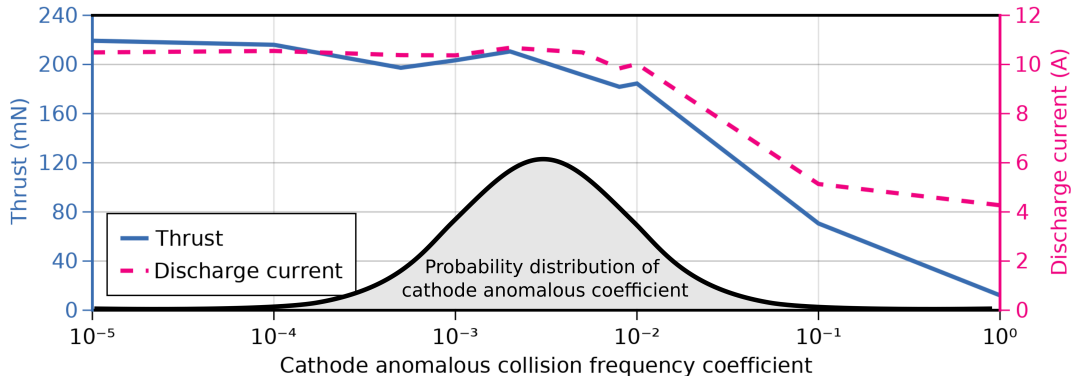


Fig. 15 Change in thrust and discharge current with increasing cathode anomalous collision frequency coefficient α . The probability distribution of α is shown in grey. All simulations performed on 300 V 15 A condition, with cathode $T_e = 5$ eV and cathode ionization fraction = 5%.

the relative magnetic field strengths of the two points. In our previous work, we implemented the anomalous collision frequency on centerline only, adopting this framework for off-centerline scaling. However, in our present work we make no such assumptions about the radial scaling. Mikellides and Lopez-Ortega[19] have demonstrated that for a static anomalous collision frequency profile applied on the thruster centerline, the off-centerline scaling does not have a significant effect on the steady-state plasma properties in Hall2De simulations. Thus, while radial effects may play some role in the discrepancy between our present results and our previous work, they are unlikely to be the sole cause.

The second possible reason stems from the noise model we have used for model calibration. In addition to allowing a larger amount of variance than the previous work, our model also preferentially fits the minimum of the anomalous collision frequency and fits $\log_{10}(\nu_{AN})$ instead of ν_{AN} . Given the insensitivity of the shape of the anomalous collision frequency curve to coefficient choice (as discussed in Sec. III), it is unlikely that the second factor impacts the solution much, but the increase in overall variance means our simulations explore a much wider range of coefficients than in the previous work, suggesting that the results seen in the previous work may have only been representative of a small region of the parameter space.

D. Implications for validity of this data-driven closure model

Although the model investigated in this work can predict the time-averaged anomalous collision frequency profile of a number of thrusters, including those not in its training data[15], it is unable to produce quantitatively accurate predictions when implemented self-consistently into a Hall thruster code. This suggests that calibrating a model based on time-averaged surrogate thruster data may be insufficient to guarantee good predictive performance. This work has shown that the plasma is very sensitive to the shape of the anomalous collision frequency profile, so small deviations from the inferred profile, particularly in the acceleration region, could yield large differences in behavior. In addition, feedback between the plasma and anomalous collision frequency model may exacerbate any small differences that exist at the start of the simulation. This possibility is supported by the wide range of possible oscillations that this model produces (Fig. 13) and suggests that suggests that a time-resolved component to the calibration may be important to obtain the correct behavior.

E. Implications for exploring other closure models

The computational infrastructure built in support of this work will enable the exploration and evaluation of many other closure models for the anomalous collision frequency. In calibrating the model for this work, we built a generalizable inference tool which can infer model coefficient distributions using the methods outlined in Sec. III and available thruster data. This tool works for zero-equation closures similar to that investigated here as well as for closures employing multiple partial differential equations. In addition, we now have developed the capability of running hundreds of Hall2De processes simultaneously, enabling rapid characterization of the impact of closure model coefficients on thruster performance. Given the large number of data-driven and physics-based closure models for the anomalous collision frequency left to be investigated[15], the ability to rapidly calibrate and evaluate such models will prove indispensable

in attempting to find one which can yield qualitatively-accurate predictions.

VI. Conclusion

In this work, we sought out to probabilistically evaluate the predictive quality of a data-driven model of the Hall thruster anomalous collision frequency, motivated by a desire to predict the performance of a thruster from operating conditions and geometry alone. To this end, we incorporated this model into a state-of-the-art fluid code and ran simulations on a magnetically-shielded thruster at five different operating conditions. At each operating condition, we ran $O(100)$ simulations, each with a different set of model coefficients sampled from a precalibrated distribution.

We have shown that such a model can produce convergent solutions for a thruster not in its training dataset over a wide variety of operating conditions. That is, the model is self-consistent and fully predictive. Moreover, the model we investigated was able to accurately predict the trends in performance metrics and oscillations with respect to increasing mass flow rate and discharge voltage. Generally, however, the model under-predicted thrust and over-predicted discharge current, resulting in low simulated anode efficiencies. The model also produced a much more protracted acceleration region than experimental data show, leading to shallow cross-field gradients, low divergence efficiency and low mass utilization efficiency compared to experiment. The major implication of this finding is that even though the data-driven model matches surrogate training data with a high degree of fidelity, its self-consistent implementation gives rise to predictions that deviate from experimental observation.

With that said, while the data-driven model tested in this work may not have quantitatively matched experimental results, the infrastructure and procedures developed for this work will permit the testing of a wide variety of additional models, accelerating the search for one which might be able to achieve the goal of performance predictions from geometry and operating conditions alone. Despite some limitations with the current work, this data-driven approach remains a promising method for developing and evaluating models for the anomalous collision frequency.

Acknowledgements

The authors would like to thank Leanne Su and Matthew Byrne for providing experimental reference data for the H9. Much of the computation performed in this work was done on the Great Lakes cluster, managed by Advanced Research Computing, a division of the University of Michigan's Information and Technology Services. Part of this work was done in Julia 1.6.0[45] and made use of the following open-source packages: Makie.jl[46], Optim.jl[47], Measurements.jl[48], FFTW.jl[49], QuadGK.jl[50], and BenchmarkTools.jl[51]. This work was supported by the Air Force Office of Scientific Research, Space Propulsion and Power Portfolio, FA9550-19-1-0022. Part of the research was carried out at the Jet Propulsion Laboratory, California Institute of Technology, under a contract with the National Aeronautics and Space Administration (80NM0018D0004).

Appendix A: Supplementary figures at other conditions

In this section, we present histograms of performance quantities and probabilistic predictions of centerline plasma properties for the 300 V and 15 A, 300 V and 20 A, 500 V and 15 A, and 600 V and 15 A conditions. As noted in the body of the work, the variance in the predictions at these conditions, particularly in the thruster acceleration region, is significantly higher than at the 300 V and 15 A condition.

A. 300 V and 15 A

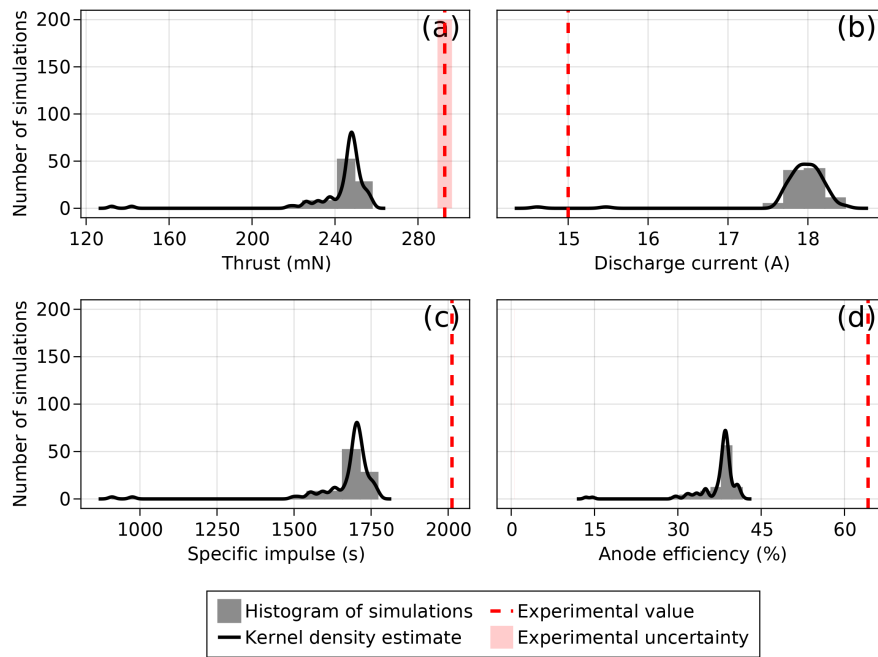


Fig. 16 Histograms of performance metrics at the 400 V and 15 A condition

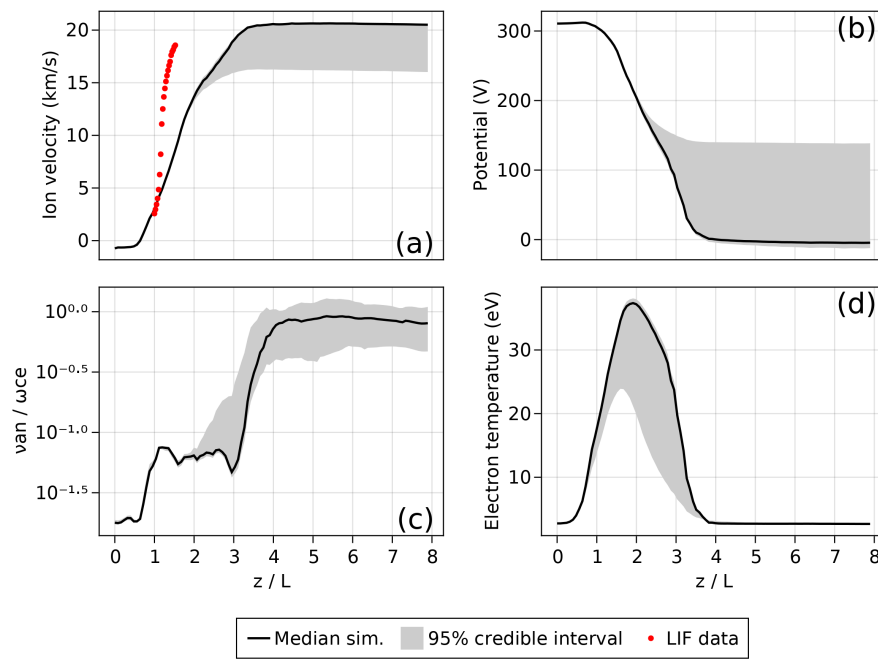


Fig. 17 Simulated centerline profiles of a) ion velocity, b) potential, c) normalized anomalous collision frequency and d) electron temperature at the 400 V and 15 A condition. Ion axial velocity data obtained via laser-induced fluorescence is depicted as a dashed red line in (a)

B. 300 V and 20 A

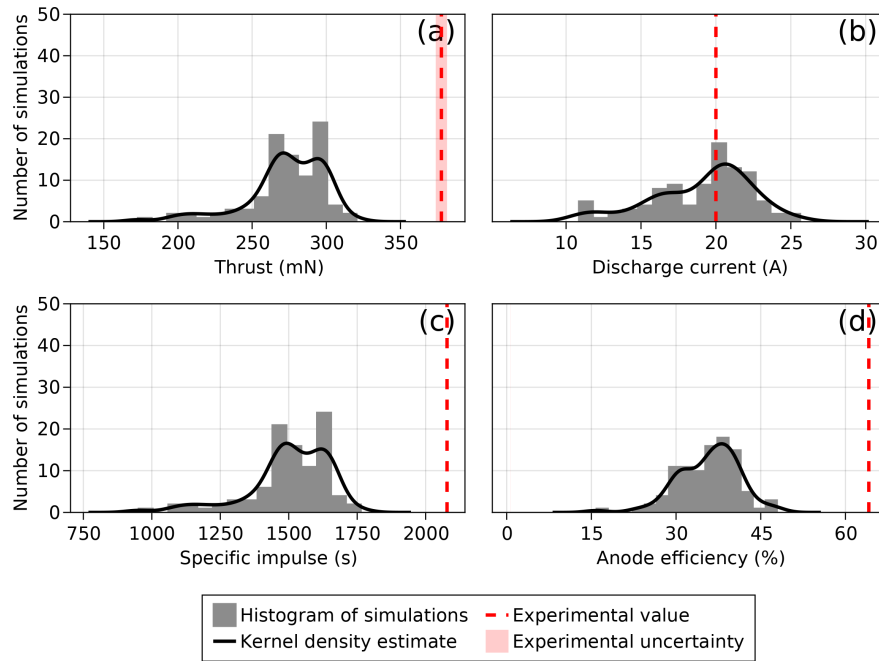


Fig. 18 Histograms of performance metrics at the 300 V and 20 A condition

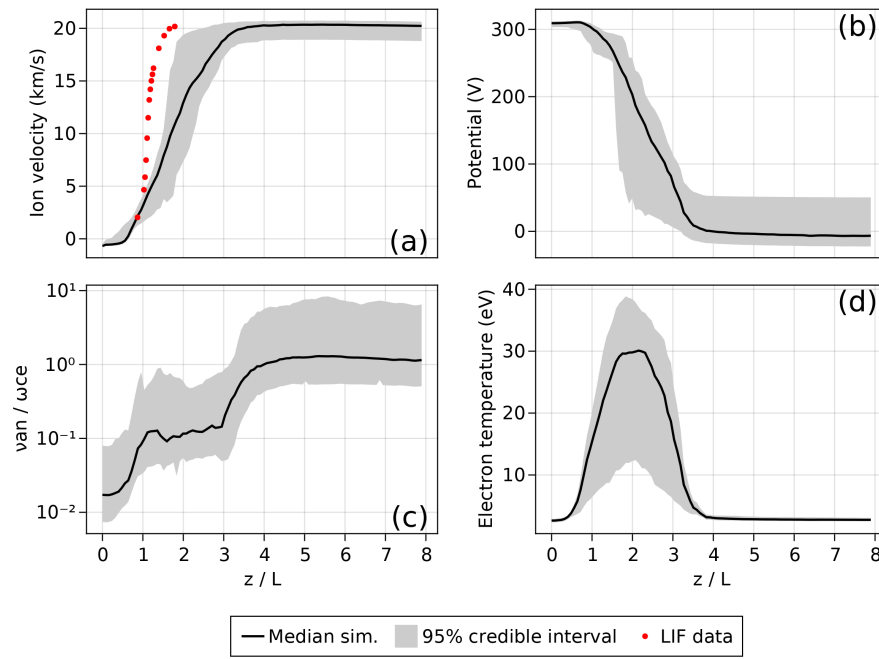


Fig. 19 Simulated centerline profiles of a) ion velocity, b) potential, c) normalized anomalous collision frequency and d) electron temperature at the 300 V and 20 A condition. Ion axial velocity data obtained via laser-induced fluorescence is depicted as a dashed red line in (a)

C. 500 V and 15 A

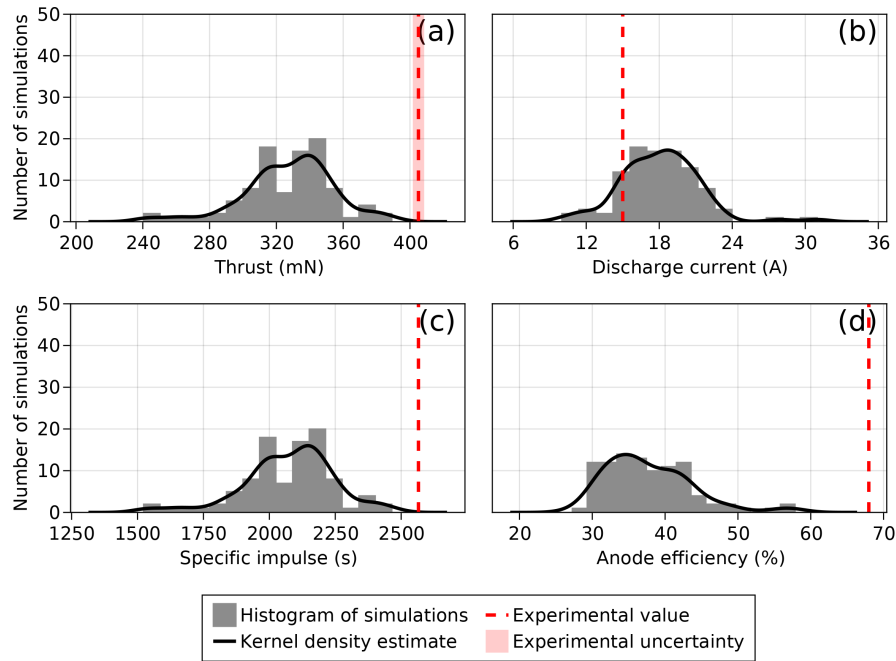


Fig. 20 Histograms of performance metrics at the 500 V and 15 A condition

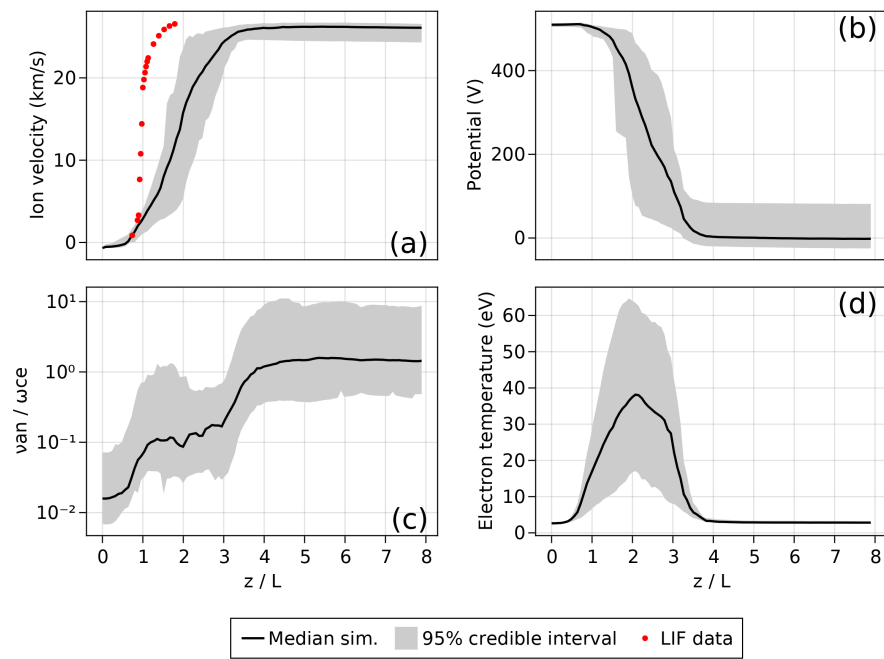


Fig. 21 Simulated centerline profiles of a) ion velocity, b) potential, c) normalized anomalous collision frequency and d) electron temperature at the 500 V and 15 A condition. Ion axial velocity data obtained via laser-induced fluorescence is depicted as a dashed red line in (a)

D. 600 V and 15 A

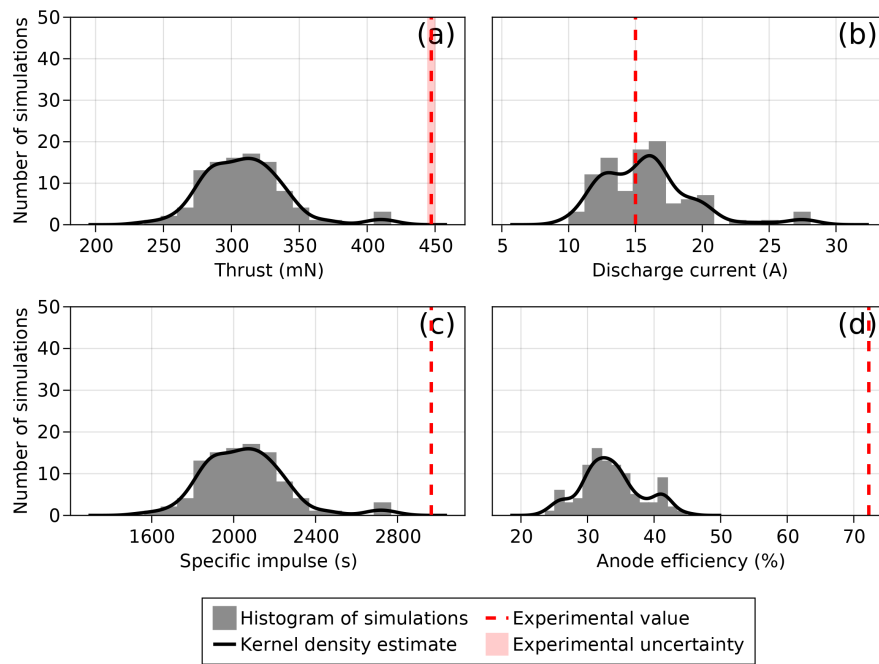


Fig. 22 Histograms of performance metrics at the 600 V and 15 A condition

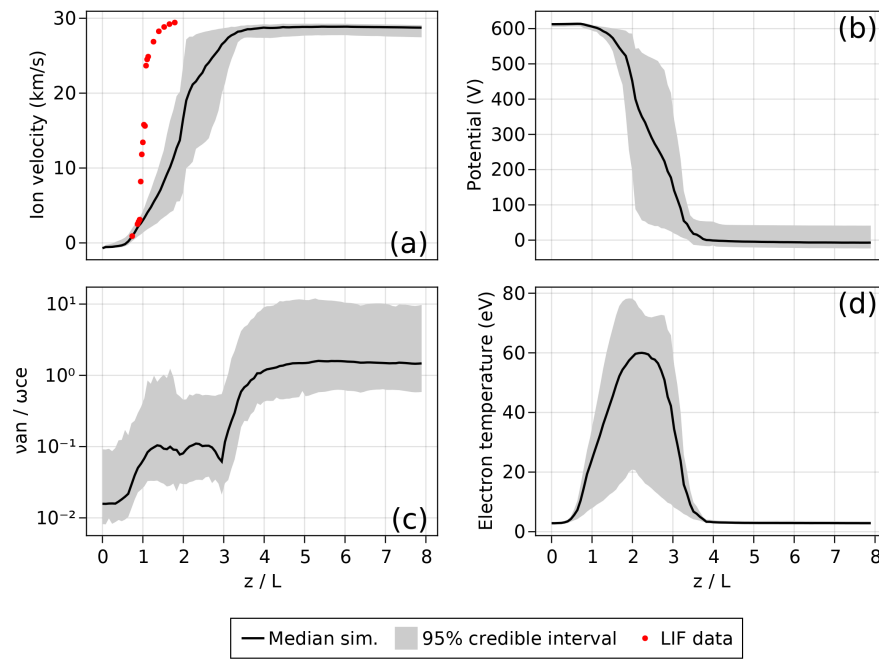


Fig. 23 Simulated centerline profiles of a) ion velocity, b) potential, c) normalized anomalous collision frequency and d) electron temperature at the 600 V and 15 A condition. Ion axial velocity data obtained via laser-induced fluorescence is depicted as a dashed red line in (a)

Appendix B: Results of cathode boundary sensitivity study

Here, we present the results of a sensitivity study carried out to help determine appropriate cathode plasma boundary conditions. We show in Fig. 24a that increasing the cathode electron temperature by 2.5 eV increases the thrust by just 5 mN, and the discharge current by only 0.2 A. In Fig. 24b, we show that increasing the cathode ionization fraction (defined as the ratio of ion to total mass flow rate exiting the cathode) has a negligible impact on the performance quantities for ratios, with the thrust increasing by 5 mN and the discharge current by 0.1 A for an increase of a factor of 1000 in the cathode ionization fraction. These results indicate that the choice of these parameters is unimportant in determining the overall plasma solution and thruster performance, so the choices made for this work ($T_e = 5$ eV and $\dot{m}_i/\dot{m} = 0.05$) are reasonable and unlikely to be significant.

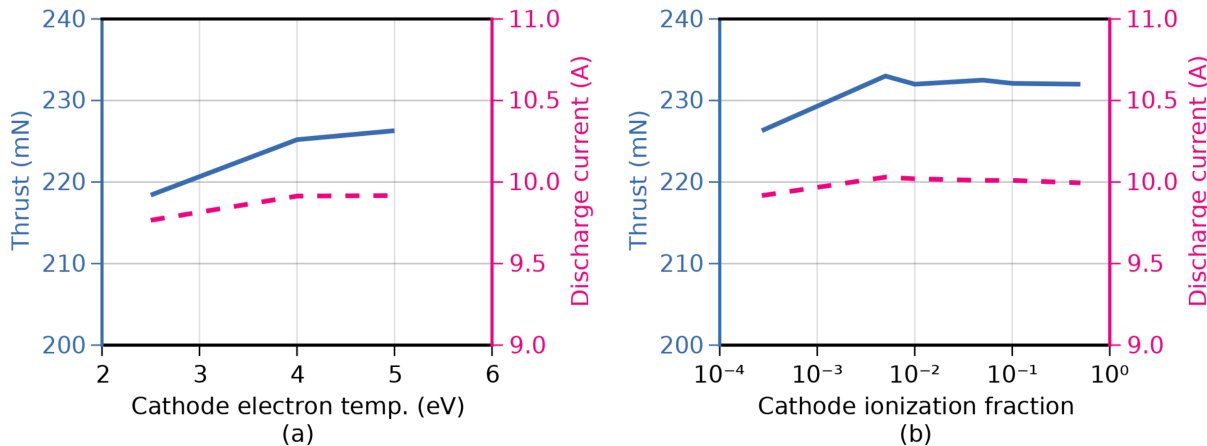


Fig. 24 Variance of the thrust and discharge current with (a) changing cathode boundary electron temperature, and (b) changing cathode ion to neutral mass flow rate ratio. All other parameters were held constant, and the cathode anomalous collision frequency coefficient was fixed at 0.001

References

- [1] Snyder, J. S., Goebel, D. M., Chaplin, V., Lopez Ortega, A., Mikellides, I. G., Aghazadeh, F., Johnson, J., Kerl, T., and Lenguito, G., “Electric Propulsion for the Psyche Mission,” *36th International Electric Propulsion Conference*, 2019.
- [2] Hofer, R. R., Kamhawi, H., Herman, D. A., Polk, J. E., Snyder, J. S., Mikellides, I. G., Huang, W., Myers, J. L., Yim, J. T., Williams, G. J., Ortega, A. L., Jorns, B. A., Sekerak, M. J., Griffith, C., Shastry, R., Haag, T. W., Verhey, T., Gilliam, B., Katz, I., Goebel, D. M., Anderson, J. R., Gilland, J. H., and Clayman, L., “Development Approach and Status of the 12.5 kW HERMeS Hall Thruster for the Solar Electric Propulsion Technology Demonstration Mission,” *34th International Electric Propulsion Conference*, 2015.
- [3] Frieman, J. D., Kamhawi, H., Huang, W., Mackey, J., Ahern, D. M., Peterson, P. Y., Gilland, J., Hall, S. J., Hofer, R. R., Inaba, D., Dao, H., Zubair, J., Neuhoff, J., and Branch, N. A., “Characterization test of the 12.5-kw advanced electric propulsion system engineering test unit hall thruster,” *AIAA Propulsion and Energy 2020 Forum*, 2020. <https://doi.org/10.2514/6.2020-3626>.
- [4] Hofer, R., Katz, I. J., Hofer, R. R., Goebel, D. M., Mikellides, I. G., and Katz, I., “Magnetic shielding of a laboratory Hall thruster. II. Experiments,” *Article in Journal of Applied Physics*, Vol. 115, 2014, p. 43304. <https://doi.org/10.1063/1.4862314>, URL [http://scitation.aip.org/content/aip/journal/jap/115/4?ver=pdfcov](http://dx.doi.org/10.1063/1.4862314http://scitation.aip.org/content/aip/journal/jap/115/4?ver=pdfcov).
- [5] Mikellides, I. G., Katz, I., Hofer, R. R., and Goebel, D. M., “Magnetic shielding of a laboratory Hall thruster. I. Theory and validation,” *Journal of Applied Physics*, Vol. 115, No. 4, 2014, p. 043303. <https://doi.org/10.1063/1.4862313>, URL <http://aip.scitation.org/doi/10.1063/1.4862313>.
- [6] De Grys, K., Mathers, A., Welander, B., and Khayms, V., “Demonstration of 10,400 hours of operation on a 4.5 kW qualification model Hall thruster,” *46th AIAA/ASME/SAE/ASEE Joint Propulsion Conference and Exhibit*, 2010. <https://doi.org/10.2514/6.2010-6698>, URL <http://arc.aiaa.org>.

- [7] Boeuf, J. P., "Tutorial: Physics and modeling of Hall thrusters," *Journal of Applied Physics*, Vol. 121, No. 1, 2017. <https://doi.org/10.1063/1.4972269>.
- [8] Tsikata, S., Lemoine, N., Pisarev, V., and Gfsillon, D. M., "Dispersion relations of electron density fluctuations in a Hall thruster plasma, observed by collective light scattering," *Physics of Plasmas*, Vol. 16, No. 3, 2009, p. 33506. <https://doi.org/10.1063/1.3093261>, URL <https://doi.org/10.1063/1.3093261>.
- [9] Esipchuk, Y. V., and Tilinin, G. N., "Drift Instability in a Hall-Current Plasma Accelerator." *Sov Phys Tech Phys*, Vol. 21, No. 4, 1976, pp. 417–423.
- [10] Scharfe, M. K., Thomas, C. A., Scharfe, D. B., Gascon, N., Cappelli, M. A., and Fernandez, E., "Shear-based model for electron transport in hybrid Hall thruster simulations," *IEEE Transactions on Plasma Science*, Vol. 36, No. 5 PART 1, 2008, pp. 2058–2068. <https://doi.org/10.1109/TPS.2008.2004364>.
- [11] Cappelli, M. A., Young, C. V., Cha, E., and Fernandez, E., "A zero-equation turbulence model for two-dimensional hybrid Hall thruster simulations," *Physics of Plasmas*, Vol. 22, No. 11, 2015. <https://doi.org/10.1063/1.4935891>.
- [12] Lafleur, T., Baalrud, S. D., and Chabert, P., "Theory for the anomalous electron transport in Hall effect thrusters. I. Insights from particle-in-cell simulations," *Physics of Plasmas*, Vol. 23, No. 5, 2016. <https://doi.org/10.1063/1.4948495>.
- [13] Lafleur, T., Baalrud, S. D., and Chabert, P., "Theory for the anomalous electron transport in Hall effect thrusters. II. Kinetic model," *Physics of Plasmas*, Vol. 23, No. 5, 2016, p. 11101. <https://doi.org/10.1063/1.4948496>, URL <http://dx.doi.org/10.1063/1.4948496>.
- [14] Jorns, B. A., "Two Equation Closure Model for Plasma Turbulence in a Hall Effect Thruster," *36th International Electric Propulsion Conference*, 2019, pp. 1–12.
- [15] Jorns, B., "Predictive, data-driven model for the anomalous electron collision frequency in a Hall effect thruster," *Plasma Sources Science and Technology*, Vol. 27, No. 10, 2018. <https://doi.org/10.1088/1361-6595/aae472>.
- [16] Jorns, B. A., Marks, T. A., and Dale, E., "A predictive hall thruster model enabled by data-driven closure," *AIAA Propulsion and Energy 2020 Forum*, American Institute of Aeronautics and Astronautics Inc, AIAA, 2020, pp. 1–17. <https://doi.org/10.2514/6.2020-3622>, URL <https://arc.aiaa.org/doi/abs/10.2514/6.2020-3622>.
- [17] Mikellides, I. G., and Katz, I., "Numerical simulations of Hall-effect plasma accelerators on a magnetic-field-aligned mesh," *Physical Review E*, Vol. 86, No. 4, 2012. <https://doi.org/10.1103/PhysRevE.86.046703>.
- [18] Hofer, R. R., Cusson, S. E., Lobbia, R. B., and Gallimore, A. D., "The H9 Magnetically Shielded Hall Thruster," *International Electric Propulsion Conference*, 2017.
- [19] Mikellides, I. G., and Lopez Ortega, A., "Challenges in the development and verification of first-principles models in Hall-effect thruster simulations that are based on anomalous resistivity and generalized Ohm's law," *Plasma Sources Science and Technology*, Vol. 28, No. 1, 2019, p. 48. <https://doi.org/10.1088/1361-6595/aae63b>, URL <https://doi.org/10.1088/1361-6595/aae63b>.
- [20] Lopez Ortega, A., and Mikellides, I. G., "The importance of the cathode plume and its interactions with the ion beam in numerical simulations of Hall thrusters," *Physics of Plasmas*, Vol. 23, No. 4, 2016, p. 1411. <https://doi.org/10.1063/1.4947554>, URL <https://doi.org/10.1063/1.4947554>.
- [21] Georgin, M. P., and Jorns, B. A., "Transient non-classical transport in the hollow cathode plume II: evaluation of models for the anomalous collision frequency," *Plasma Sources Sci. Technol.*, Vol. 29, No. 105011, 2020. <https://doi.org/10.1088/1361-6595/abb0cf>, URL <https://doi.org/10.1088/1361-6595/abb0cf>.
- [22] Goebel, D. M., and Katz, I., *Fundamentals of Electric Propulsion: Ion and Hall Thrusters*, 2008. <https://doi.org/10.1002/9780470436448>.
- [23] Koo, J. W., and Boyd, I. D., "Modeling of anomalous electron mobility in Hall thrusters," *Physics of Plasmas*, Vol. 13, No. 3, 2006, p. 3541. <https://doi.org/10.1063/1.2172191>, URL <https://aip.scitation.org/doi/abs/10.1063/1.2172191>.
- [24] Hara, K., Sekerak, M. J., Boyd, I. D., and Gallimore, A. D., "Mode transition of a Hall thruster discharge plasma," *Journal of Applied Physics*, Vol. 115, No. 20, 2014. <https://doi.org/10.1063/1.4879896>.
- [25] Ortega, A. L., Katz, I., Mikellides, I. G., and Goebel, D. M., "Self-Consistent Model of a High-Power Hall Thruster Plume," *IEEE Transactions on Plasma Science*, Vol. 43, No. 9, 2015, pp. 2875–2886. <https://doi.org/10.1109/TPS.2015.2446411>.

- [26] Morozov, A. I., and Savel'yev, V. V., "Fundamentals of Stationary Plasma Thruster Theory," Springer, Boston, MA, 2000, pp. 203–391. https://doi.org/10.1007/978-1-4615-4309-1_2, URL https://link.springer.com/chapter/10.1007/978-1-4615-4309-1{_}2.
- [27] Barral, S., Makowski, K., Peradzyński, Z., Gascon, N., and Dudeck, M., "Wall material effects in stationary plasma thrusters. II. Near-wall and in-wall conductivity," *Physics of Plasmas*, Vol. 10, No. 10, 2003, pp. 4137–4152. <https://doi.org/10.1063/1.1611881>, URL <http://aip.scitation.org/doi/10.1063/1.1611881>.
- [28] Mikellides, I. G., Katz, I., Goebel, D. M., and Jameson, K. K., "Evidence of nonclassical plasma transport in hollow cathodes for electric propulsion," *J. Appl. Phys.*, Vol. 101, 2007, p. 63301. <https://doi.org/10.1063/1.2710763>, URL <https://doi.org/10.1063/1.2710763>.
- [29] Jorns, B. A., Mikellides, I. G., and Goebel, D. M., "Ion acoustic turbulence in a 100-A LaB6 hollow cathode," *Physical Review E - Statistical, Nonlinear, and Soft Matter Physics*, Vol. 90, No. 6, 2014. <https://doi.org/10.1103/PhysRevE.90.063106>.
- [30] Jorns, B. A., Cusson, S. E., Brown, Z., and Dale, E., "Non-classical electron transport in the cathode plume of a Hall effect thruster," *Physics of Plasmas*, Vol. 27, No. 2, 2020, p. 22311. <https://doi.org/10.1063/1.5130680>, URL <https://doi.org/10.1063/1.5130680>.
- [31] Sagdeev, R. Z., "The 1976 Oppenheimer lectures: Critical problems in plasma astrophysics. I. Turbulence and nonlinear waves," *Reviews of Modern Physics*, 1979. <https://doi.org/10.1103/RevModPhys.51.1>.
- [32] TSytovich, V. N., and Haar, D. T., *Lectures on non-linear plasma kinetics*, Springer, Berlin, 1995.
- [33] Woods, L. C., *Principles of Magnetoplasma dynamics*, Oxford, England, ????
- [34] Hutter, F., Hoos, H., and Leyton-Brown, K., "An efficient approach for assessing hyperparameter importance," *31st International Conference on Machine Learning, ICML 2014*, Vol. 2, 2014, pp. 1130–1144.
- [35] Feurer, M., and Hutter, F., "Hyperparameter Optimization," *Automated Machine Learning: Methods, Systems, Challenges*, edited by F. Hutter, L. Kotthoff, and J. Vanschoren, Springer, 2019, Chap. 1, pp. 3–33. https://doi.org/10.1007/978-3-030-05318-5_1, URL <http://www.springer.com/series/15602>.
- [36] Yang, L., and Shami, A., "On hyperparameter optimization of machine learning algorithms: Theory and practice," *Neurocomputing*, Vol. 415, 2020, pp. 295–316. <https://doi.org/10.1016/j.neucom.2020.07.061>.
- [37] Haario, H., Laine, M., Mira, A., and Saksman, E., "DRAM: Efficient adaptive MCMC," *Statistics and Computing*, Vol. 16, No. 4, 2006, pp. 339–354. <https://doi.org/10.1007/s11222-006-9438-0>, URL <https://link.springer.com/article/10.1007/s11222-006-9438-0>.
- [38] Georgin, M. P., Jorns, B. A., and Gallimore, A. D., "Transient non-classical transport in the hollow cathode plume I: measurements of time-varying electron collision frequency Transient non-classical transport in the hollow cathode plume I: measurements of time-varying electron collision frequency," *Plasma Sources Sci. Technol.*, Vol. 29, 2020, p. 13. <https://doi.org/10.1088/1361-6595/abb0ce>, URL <https://doi.org/10.1088/1361-6595/abb0ce>.
- [39] Cusson, S. E., Hofer, R. R., Lobbia, R. B., Jorns, B. A., and Gallimore, A. D., "Performance of the H9 Magnetically Shielded Hall Thrusters," *International Electric Propulsion Conference*, 2017.
- [40] Su, L. L., and Jorns, B. A., "Performance at High Current Densities of a Magnetically-Shielded Hall Thruster," *AIAA Propulsion and Energy 2021 Forum*, 2021.
- [41] Katz, I., and Mikellides, I. G., "Neutral gas free molecular flow algorithm including ionization and walls for use in plasma simulations," *Journal of Computational Physics*, Vol. 230, No. 4, 2011, pp. 1454–1464. <https://doi.org/10.1016/J.JCP.2010.11.013>.
- [42] Hofer, R. R., "Development and Characterization of High-Efficiency, High-Specific Impulse Xenon Hall Thrusters," *University of Michigan Plasmadynamics and Electric Propulsion Laboratory*, Vol. Ph.D. Diss, No. 358, 2004.
- [43] Dale, E., "Investigation of the Hall Thruster Breathing Mode," Phd, University of Michigan, 2019.
- [44] Giannetti, V., Saravia, M. M., and Andreussi, T., "Measurement of the breathing mode oscillations in Hall thruster plasmas with a fast-diving triple Langmuir probe," *Physics of Plasmas*, Vol. 27, No. 12, 2020, p. 123502. <https://doi.org/10.1063/5.0022928>, URL <http://aip.scitation.org/doi/abs/10.1063/5.0022928>.
- [45] Bezanson, J., Edelman, A., Karpinski, S., and Shah, V. B., "Julia: A fresh approach to numerical computing," *SIAM Review*, Vol. 59, No. 1, 2017, pp. 65–98. <https://doi.org/10.1137/141000671>, URL <https://pubs.siam.org/doi/10.1137/141000671>.

- [46] Simon, Jkrumbiegel, Singhvi, A., Wang, A., Freyer, F., Vertechi, P., Holy, T., Borregaard, M. K., Datseris, G., M, M., Greimel, F., Butterworth, I., Foster, C., Dehaybe, H., Schauer, M., Kilpatrick, L., Byrne, S., Widmann, D., Kragol, Weidner, J., Sharma, A., Micluța-Câmpeanu, S., Hatherly, M., Herikstad, R., Goretkin, G., TagBot, J., Štih, V., Smldis, and Ponet, L., “JuliaPlots/Makie.jl: v0.14.2,” , jun 2021. <https://doi.org/10.5281/zenodo.5034803>, URL <https://doi.org/10.5281/zenodo.5034803>.
- [47] Mogensen, P. K., and Riseth, A. N., “Optim: A mathematical optimization package for {Julia},” *Journal of Open Source Software*, Vol. 3, No. 24, 2018, p. 615. <https://doi.org/10.21105/joss.00615>.
- [48] Giordano, M., “Uncertainty propagation with functionally correlated quantities,” , oct 2016. URL <https://arxiv.org/abs/1610.08716>.
- [49] Frigo, M., and Johnson, S., “The Design and Implementation of {FFTW3},” *Proceedings of the IEEE*, Vol. 93, No. 2, 2005, pp. 216–231. <https://doi.org/10.1109/JPROC.2004.840301>.
- [50] Johnson, S. G., “{QuadGK.jl}: {G}auss-{K}ronrod integration in {J}ulia,” \url{<https://github.com/JuliaMath/QuadGK.jl>}, ????
- [51] Chen, J., and Revels, J., “Robust benchmarking in noisy environments,” , aug 2016. URL <https://arxiv.org/abs/1608.04295>.